



MR to ultrasound registration for image-guided prostate interventions

Yipeng Hu^{a,*}, Hashim Uddin Ahmed^b, Zeike Taylor^a, Clare Allen^c, Mark Emberton^b, David Hawkes^a, Dean Barratt^a

^a Centre for Medical Image Computing, University College London, London, UK

^b Department of Urology, Division of Surgery & Interventional Science, University College London, London, UK

^c Department of Radiology, University College London Hospital, London, UK

ARTICLE INFO

Article history:

Available online 13 December 2010

Keywords:

Image registration
Biomechanical modelling
Statistical shape modelling
Minimum-invasive interventions
Prostate cancer

ABSTRACT

A deformable registration method is described that enables automatic alignment of magnetic resonance (MR) and 3D transrectal ultrasound (TRUS) images of the prostate gland. The method employs a novel “model-to-image” registration approach in which a deformable model of the gland surface, derived from an MR image, is registered automatically to a TRUS volume by maximising the likelihood of a particular model shape given a voxel-intensity-based feature that represents an estimate of surface normal vectors at the boundary of the gland. The deformation of the surface model is constrained by a patient-specific statistical model of gland deformation, which is trained using data provided by biomechanical simulations. Each simulation predicts the motion of a volumetric finite element mesh due to the random placement of a TRUS probe in the rectum. The use of biomechanical modelling in this way also allows a dense displacement field to be calculated within the prostate, which is then used to non-rigidly warp the MR image to match the TRUS image. Using data acquired from eight patients, and anatomical landmarks to quantify the registration accuracy, the median final RMS target registration error after performing 100 MR–TRUS registrations for each patient was 2.40 mm.

© 2010 Elsevier B.V. All rights reserved.

1. Introduction

1.1. Background

Prostate cancer is a major international health problem with a large and rising incidence in many parts of the world. In several regions, including the USA, Australia, New Zealand, and Western and Northern Europe, prostate cancer is now the most commonly diagnosed non-cutaneous malignancy in men and a leading cause of cancer-related death. In the USA, for example, it is estimated that in 2009 there will be 192,280 new cases of prostate cancer, accounting for a quarter of all new (non-cutaneous) cancer diagnoses, and 27,360 deaths from prostate cancer (Jemal et al., 2009).

Transrectal ultrasound (TRUS) imaging of the prostate gland is the routine clinical standard method for guiding needle biopsy and modern minimally-invasive surgical interventions for the treatment of prostate cancer. Currently available minimally-invasive interventions include brachytherapy, cryotherapy, intensity-modulated radiotherapy, high-intensity focused ultrasound (HIFU), photothermal ablation (Lindner et al., 2010) and photodynamic therapy (Aus, 2006; Marberger et al., 2008). TRUS

guidance has several advantages in that it does not involve ionising radiation, is simple to perform, widely accessible, and inexpensive. However, tumours are often difficult or impossible to accurately distinguish in standard B-mode TRUS images (Terris et al., 1997). Furthermore, navigation using standard B-mode TRUS imaging is limited to using 2D views, which means that accurate localisation of target regions can be technically very difficult, especially for inexperienced operators.

Recently, the use of microbubble contrast agents has been demonstrated to increase the sensitivity and tumour detection rate compared with conventional B-mode ultrasound (Halpern et al., 2005; Yang et al., 2008). Ultrasound (US)-based tissue characterisation and elastography have also been the subject of recent attention (Braeckman et al., 2008; Moradi et al., 2007; Salomon et al., 2008; Zhang et al., 2008), but further clinical evaluation is required to fully establish the value of these methods. The accuracy of magnetic resonance (MR) imaging for the localisation and characterisation of prostate cancer, on the other hand, has been a focus for significant research activity in recent years. MR is now widely considered to be the most promising imaging modality for non-invasive identification of prostate cancer. A recent systematic review of this technique reports a sensitivity of between 60% and 96% for localising prostate cancer using T2-weighted MR imaging combined with an endorectal coil (Kirkham et al., 2006). A prospective multicenter study, conducted by the American College

* Corresponding author.

E-mail address: yipeng.hu@ucl.ac.uk (Y. Hu).

of Radiology Imaging Network and published since the review of Kirkham et al. (2006), reports an area under the ROC curve of between 0.58 and 0.63 for the sextant localisation of peripheral zone cancer using T2-weighted MR imaging alone with a 1.5 T pelvic phased-array coil (Weinreb et al., 2009). Although this study found no significant difference between standard MR imaging and MR spectroscopy in terms of cancer localisation accuracy, several other studies in the literature have convincingly demonstrated that imaging at higher field strengths (in particular 3 T) and/or the addition of one or more functional MR imaging techniques, such as dynamic contrast enhanced (DCE), diffusion-weighted (DW) imaging or MR spectroscopy, can significantly improve detection accuracy (Futterer, 2007; Kirkham et al., 2006; Ravizzini et al., 2009; Villers et al., 2006, 2009).

It should be noted, however, that at present the specificity of MR imaging for localising prostate cancer is not sufficiently high to replace needle biopsy as the gold standard test for prostate cancer, and therefore histological verification is still required. Nevertheless, MR imaging has emerged as a potentially powerful tool for localising suspicious regions within the prostate gland. Once identified, tumours localised using MR imaging can be targeted during biopsy, given the availability of sufficiently accurate image guidance technology. Furthermore, the detailed information on the 3D spatial distribution of disease, the presence or absence of extracapsular extension, involvement of the seminal vesicles, and patient-specific pelvic anatomy provided by MR imaging, combined with localised histological information provided by biopsy, are extremely powerful tools for clinical management and subsequent therapy planning (Ahmed et al., 2009a).

Recently, there has been growing clinical interest in targeted therapy strategies in which only part of the prostate gland is treated in order to minimise damage to vulnerable structures, such as nerves, whilst maintaining adequate disease control (Ahmed et al., 2007, 2009b; Eggener et al., 2007; Scardino and Abenham, 2008). The principal motivation for such approaches is the potential for a reduced risk of side-effects compared with traditional “whole-gland” interventions (Ahmed et al., 2007, 2009c; Eggener et al., 2007). Implementing focal or tissue-sparing therapies is highly problematic since they rely critically on the availability of an accurate method for mapping disease as well as precise (image-guided) delivery technology. In terms of disease mapping, the current gold standard is transperineal template-guided saturation biopsy in which 20–50 tissue samples are collected systematically at 5 mm intervals using a template grid and TRUS guidance (Onik and Barzell, 2008; Pinkstaff et al., 2005). This technique is, however, very invasive compared to freehand transrectal biopsy, which is used routinely for diagnostic purposes, and is usually performed under general anaesthesia to minimise patient discomfort and distress (Pinkstaff et al., 2005).

In this paper, we are primarily concerned with using information provided by MR images to target biopsy or an interventional procedure. We refer to such procedures as MR-targeted procedures. In such procedures, MR images are used to localise and determine the extent and stage of disease prior to a procedure. This information, possibly in conjunction with additional information, such as previous biopsy findings, is then used to preferentially target tissue regions suspected of harbouring disease. MR-based targeting has been adopted in a number of prostate cancer applications, including biopsy (Barnes et al., 2005; Lattouf et al., 2007; Hambrook et al., 2008, 2010); brachytherapy (Clarke et al., 2002; Barnes et al., 2005), HIFU (Emberton et al., 2007), photothermal therapy (Lindner et al., 2009), and photodynamic therapy (Trachtenberg et al., 2008).

This approach may be distinguished from MR-guided procedures, which are performed inside an MR scanner and may or may not employ MR imaging for the purposes of targeting

(Pondman et al., 2008; Tempny et al., 2008). MR-guided procedures are technically demanding and require special-purpose, MR-compatible equipment and instruments. In particular, performing a procedure within a closed-bore, diagnostic MR scanners in particular is technically challenging given the limited access to patient. Consequently, robotic devices must be employed to accurately manipulate instruments in the confined space. In contrast, patient access is much easier within an open MR scanner, designed specifically for interventional procedures, but the image quality is generally too poor to be useful for accurate targeting. Therefore, if MR targeting is required, diagnostic-quality MR images must first be obtained using a diagnostic scanner and registered to the images obtained during the procedure. In both cases, image acquisition is slow compared with TRUS imaging and realtime guidance is currently not possible. Moreover, despite the fact that MR imaging facilities are undoubtedly becoming more widely available in hospitals, MR guidance remains a high cost solution that is currently practical only in a relatively small number of specialist centres.

MR-targeted biopsy can be performed using either a transrectal or transperineal approach and potentially offers a much less invasive alternative to conventional TRUS-guided biopsy schemes, since far fewer tissue samples are typically required when only a small number of suspicious regions are sampled. The technique also has the potential to improve the cancer detection rate in patients with a strong suspicion of prostate cancer, but in whom have had one or more negative TRUS-guided biopsies (Hambrook et al., 2010). Furthermore, since there is a much greater likelihood of obtaining samples near to the centre of a tumour, grading accuracy may be improved. Important applications include: monitoring patients undergoing active surveillance, post-treatment evaluation, and the validation of novel diagnostic imaging techniques. In patients with localised disease, the same MR-targeted approach can be applied to deliver minimally-invasive interventions using a treatment plan based on information derived from MR images, with or without co-registered biopsy data.

A practical and low-cost solution that motivates the contributions of this paper is an MR-targeted, TRUS-guided approach in which TRUS is the primary guidance modality, but MR images obtained prior to a procedure (possibly together with a surgical plan) are registered to the TRUS images obtained during a procedure (Kaplan et al., 2002). This approach has the advantage that the standard TRUS guidance platform is preserved, but is complicated by the significant gland motion (including deformation) that can often occur between MR and TRUS imaging (Byrne, 2005). Therefore, it is highly desirable that the registration method compensates for this effect to achieve the highest possible accuracy. Prostate motion can arise from a number of causes, including bladder filling, rectal wall motion, changes in patient position (e.g. supine versus lithotomy), placement of an endorectal coil during MR imaging, and from the placement of the TRUS probe during an intervention. A second requirement is that, during an intervention, the registration procedure should be as fast as possible and avoid significant user-interaction.

1.2. Related work

To date, there are a number of deformable registration methods described in the literature that have been applied to the problem of registering MR images of the prostate acquired at different times, with and without using an endorectal coil (Alterovitz et al., 2006; Baowei et al., 2003; Bharatha et al., 2001; du Bois et al., 2004). In the work of Alterovitz et al. (2006), Bharatha et al. (2001), and Hensel et al. (2007), a biomechanical model is used to constrain the allowable deformations to be physically plausible. Crouch et al. (2007) describe a method for automatically generating a

volumetric FE mesh of the prostate gland, together with appropriate boundary conditions, and validate the method for registration using CT images obtained with and without an endorectal MR imaging coil in place. They also address the effect of gland swelling following brachytherapy seed implantation.

Singh et al. (2008) describe a manual method for non-rigidly registering MR and TRUS images, but this requires significant user interaction during a procedure to place control points to align both the surface and structures inside the prostate. The problem of *automatically* registering MR images to TRUS images is challenging because of the intrinsic differences in grey-level intensity characteristics between the two modalities, combined with the presence of artefacts (particularly in the TRUS images). In particular, standard intensity-based approaches, such as those based on maximising mutual information, often perform poorly since a probabilistic relationship between MR and US voxel intensities usually does not exist. Furthermore, when the transformation model is non-rigid, such approaches are computationally intensive and therefore typically require high-speed, special-purpose computer hardware and an optimised algorithmic implementation to make them practical for interventional applications.

An automatic registration technique reported by Wu et al. (2003) adopts a “marker-to-pixel” approach in which the prostate capsule surface (the “marker”), segmented from one 3D TRUS image, is rigidly registered to another TRUS image of the same patient using a novel similarity measure and a genetic algorithm optimisation scheme that aims to maximise the alignment between TRUS image gradient vectors and the surface normal vectors. Further work by Shao et al. (2006) investigated methods for registering the pubic arch in MR and TRUS images by comparing the similarity measure proposed by Wu et al. (2003) with alternative measures based on the average intensity across the surface, and on a modified surface intensity measure that takes advantage of the high intensity at the bone surface and anterior shadow artefact that is characteristic in TRUS images of the pubic arch. The latter measure was found to provide the most robust and accurate registrations of the pubic arch, but a registration error for the prostate gland itself is not reported.

More recently, Xu et al. (2008) describe a method for rigid MR-to-TRUS registration during freehand transrectal biopsy using an end-firing TRUS probe. Using CT imaging to identify needle tip locations, the accuracy of the system in localising the centres for target tumours within a prostate phantom was found to be 2.4 ± 1.2 mm. A further evaluation of the registration accuracy based on the overlap between capsule contours drawn on 2D MR and TRUS images selected from 20 patient datasets yielded a $90 \pm 7\%$ overlap following registration. No data were provided on the accuracy of registering structures within the gland, however. It is also noteworthy that the system described in this paper only compensates for motion *during* a procedure using TRUS–TRUS image registration initialised by electromagnetic tracking. An initial manual registration of the MR and TRUS images at the start of procedure is therefore required. Details of this initial registration step are unfortunately not provided.

A further phantom-based MR–TRUS registration study was carried out by Narayanan et al. (2009). Using a multimodality prostate phantom with embedded glass beads, which served as fiducial markers, they report a mean fiducial registration error of 3.06 ± 1.14 following non-rigid registration of MR and 3D TRUS images of the phantom. The registration was achieved by a deformable registration of the prostate surface, segmented from both the MR and TRUS images, followed by a linear elastic warping of the gland volume using the surface point displacements as boundary conditions.

In the method described in this paper, the same general framework as proposed previously by Davatzikos et al. (2001) and

Mohamed et al. (2002) is adopted in which a biomechanical model of soft-tissue deformation is used to provide training data for a statistical model of organ motion. A description of the method used to generate a biomechanically-constrained deformable model of the prostate gland, validated using 3D TRUS data, was previously described in Hu et al. (2008a,b). In the present work, we employ a fast non-linear finite element solver (Taylor et al., 2008) to perform training simulations using meshes derived from MR images. The primary contribution is the introduction of a novel “model-to-image” method for automatically registering the deformable prostate model surface directly to the TRUS images is also proposed. The method overcomes the problem of low signal-to-noise-ratio of the target TRUS data by formulating the registration problem in a probabilistic framework, wherein an image noise model is used to account for uncertainty in voxel-intensity-based features extracted from the TRUS images, which represent surface normal vectors of the prostate gland. Related approaches that use statistical and biomechanical priors have also been widely adopted for MR image segmentation (Heimann and Meinzer, 2009; Makni et al., 2009).

2. Methods

In this work, a patient-specific model of TRUS-probe-induced prostate motion was generated by statistical analysis of the results of simulating possible tissue deformations using finite element analysis (FEA). The volumetric FE mesh of prostate and surrounding anatomy of each patient was generated from a detailed segmentation of a high-resolution, T2-weighted diagnostic MR image. The statistical model takes the same form as the mesh, but the deformations of soft-tissue structures are constrained based on the mesh node displacement statistics of the data used to train the model. In this case, training data are generated using biomechanical simulations to predict the probe-induced motion of the prostate for a range of different combinations of boundary conditions and material properties that may be encountered during a procedure. Since these are generally unknown prior to a procedure for an individual patient, and are extremely difficult or impossible to measure *in vivo*, the statistical approach adopted enables variability and uncertainty in these parameters to be included in the deformable model; in essence, the biomechanical simulations define a subspace of possible gland motions that may be encountered in reality and force a statistical model based on these data to exhibit “physically plausible” deformations. Principal component analysis (PCA) of the FE mesh node displacements provides a convenient way to represent global variations in gland shape within this space as a low-dimensional, linear model. Consequently, the shape of the prostate predicted by the deformable model is determined by relatively few parameters.

One potential limitation of this approach is that the degree to which the range of gland motion represented by the statistical model reflects the real motion of the prostate is dependant on the accuracy of the biomechanical model in predicting realistic deformations. An important assumption underlying our approach is that the (TRUS-probe-induced) motion is described by our chosen biomechanical model with sufficient accuracy to define the motion subspace encountered during a surgical procedure. This assumption is supported by our previous work on the validation of the combined statistical-biomechanical model using 3D TRUS data (Hu et al., 2008a,b).

In our registration method, the prostate gland surface within the deformable model is fitted automatically and rapidly to a 3D TRUS volume, acquired during a procedure, by minimising a novel vector-based similarity measure so that the best alignment between the surface normals of the model and estimated surface

normals, determined from the TRUS volume, is achieved. The surface normals are estimated automatically from the TRUS image using a second-order Gaussian filter configured to enhance locally sheet-like structures (in particular, the prostate capsule surface). The use of the biomechanically-constrained statistical motion model enables registration to be achieved rapidly, which is particularly important for time-critical applications such as image-guided prostate cancer interventions. Furthermore, although only the capsule surface is aligned during the registration, the displacement of every voxel within the gland can be calculated as the model captures motion based on the displacement of every node in the FE mesh. This is particularly advantageous because corresponding MR/TRUS-visible features inside the gland, which are required for most existing non-rigid registration algorithms, are very sparse in practice.

An overview of the proposed registration method is illustrated in Fig. 1. The method involves the following two-stage scheme:

- a. *Planning stage* (performed before a surgical procedure):
 - (i) Acquire diagnostic MR image.
 - (ii) Build a patient-specific FE mesh of the prostate gland and surrounding anatomy from the MR image.
 - (iii) Perform a series of FEA simulations of gland motion using randomly sampled material properties and boundary conditions which correspond to different possible positions and orientations of the TRUS probe during the procedure.
 - (iv) Construct a SMM by applying PCA to the predicted FE mesh node displacements.
 - (v) Find the principal modes of variation of the SMM (the final shape parameters of the SMM correspond to the weights of these modes).
- b. *Registration stage* (performed during a procedure):
 - (i) Acquire a 3D TRUS volume.
 - (ii) Compute the TRUS image feature vectors using second-order Gaussian filtering.
 - (iii) Iteratively optimise the rigid-body and SMM shape parameters until the likelihood of a particular set of registration parameters, given the feature vectors derived from the TRUS image, is maximised.
 - (iv) Compute the final displacement for each MR voxel inside the FE model and warp the MR image using these displacements.

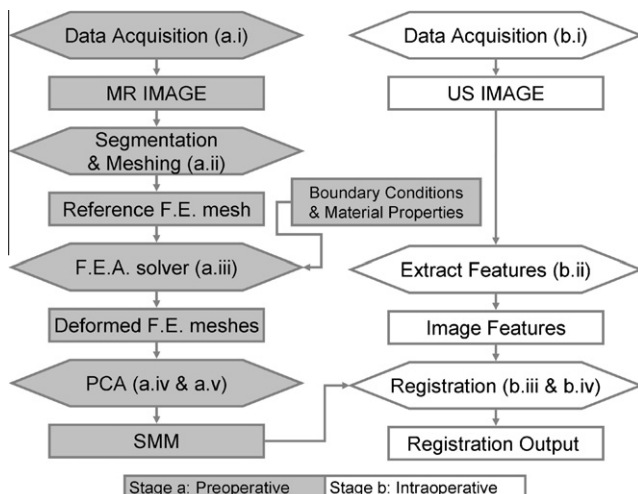


Fig. 1. An overview of the registration method. Preoperative processes and data are shaded grey, whereas intraoperative processes and data are not shaded.

A detailed description of these steps is provided in the remainder of Section 2.

2.1. Statistical motion model generation

2.1.1. Biomechanical modelling

The prostate gland motion between MR and TRUS imaging sessions involves two transformations: firstly, there is a change in patient position due to the fact that MR imaging is performed in the supine position, whilst intraoperative TRUS is generally performed in the lithotomy position. Secondly, there is a transformation due to the placement of the TRUS probe in the rectum. For simplicity, we assume that the first transformation is approximated by a rigid-body transformation of the pelvis and therefore the position and orientation of the prostate base–apex axis relative to the anus and distal section of the rectum, adjacent to the prostate, remain unchanged. This enables us to use the geometry of the prostate (and other organs) segmented from an MR image as the initial (or resting) state for the finite element simulations. However, in reality, there is likely to be some tissue motion solely due to the change in patient position, which may change the orientation of the anus and rectum relative to prostate.

We assume that the shape change of the prostate gland due to the change from the supine to lithotomy position is sufficiently small as to be captured by a model of prostate motion in which only the deformation due to the manipulation of the TRUS probe is explicitly modelled. We also assume that the range of possible orientations of the TRUS probe, modelled in the FE simulations, is wide enough to capture changes in the relative orientation of the prostate and rectum/anus that may occur when there is a change in patient position.

For the purposes of this study, diagnostic MR images were segmented by manually defining contours on transverse slices using a custom-made graphical user interface written using Matlab. The segmentation process was time-consuming (typically taking 45 min per patient), but was the most accurate method for segmenting pelvic anatomy available. The outer surface of the prostate gland capsule was segmented, and the gland itself divided into the central and peripheral zones, which are usually clearly visible in T2-weighted MR images. The pelvic bone, the rectum, and the bladder at the base of the prostate were also segmented (see Figs. 2 and 3).

Following segmentation, the capsule surface contours were initially converted into a smoothed spherical harmonic representation, which were in turn converted into a triangulated surface

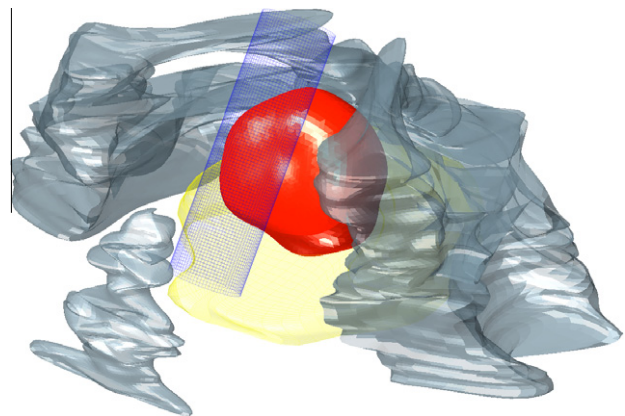


Fig. 2. An illustration of surface meshes obtained by segmenting an MR image. The TRUS probe (with sheath), approximated by a cylinder is shown in blue. The prostate gland, the pelvis, and the bladder are shown in red, grey and yellow, respectively. (For interpretation of the references to colour in this figure legend, the reader is referred to the web version of this article.)

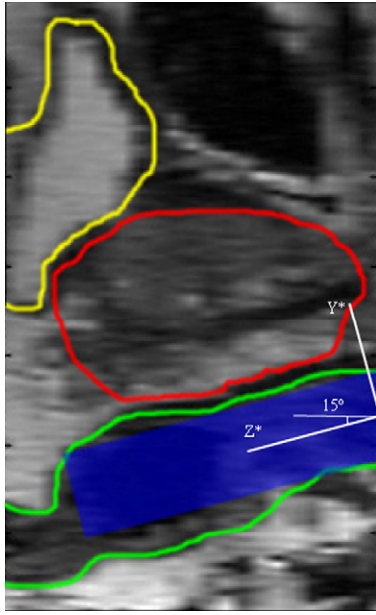


Fig. 3. An illustration of the local TRUS probe co-ordinate system shown on a sagittal prostate MR image. The prostate gland, rectal wall, probe and bladder are shown in red, green, blue and yellow, respectively. The reference local co-ordinate system was defined with the z-axis orientated at 15° relative to the cranial-caudal axis. (For interpretation of the references to colour in this figure legend, the reader is referred to the web version of this article.)

mesh using a method described by Zacharopoulos et al. (2006). A triangulated surface mesh was also generated for the pelvis. All surface data were imported into a commercial FEA software package (ANSYS v. 11, ANSYS Europe Ltd., Oxfordshire, UK), and the solid modelling tools provided by the software used to construct a FE model comprising 35–60,000 tetrahedral elements. Using the refinement tool available in ANSYS, the region around the rectum was re-meshed to obtain a high element density in this region. This enabled the TRUS probe – or more precisely, the fluid-filled sheath placed over the TRUS probe, approximated by a cylinder – to be modelled directly in each simulation without the need for re-meshing. Finally, elements within all the compartments of the FE model were labelled according to the corresponding tissue type.

Each FE model included all of the segmented organs plus an additional compartment representing the soft tissue connecting these organs (assumed to be homogeneous). All organs interact during each FE simulation, with their relative motion governed by randomly assigned elastic material properties and the boundary conditions, determined by the pose of the TRUS probe.

In the FEA simulations, all tissues were assumed to behave as isotropic, elastic materials described by a neo-Hookean model

(Zienkiewicz and Taylor, 2000). Since the values of the elastic properties were assumed to be unknown, the shear modulus (G) and bulk modulus (K) for each of the four soft-tissue compartments corresponding to the peripheral and central prostate zone, the rectum, and surrounding tissue, were assigned randomly sampled values within the physiological ranges given in Table 1. The usual condition of incompressibility was not assumed because it can be argued that this might not be appropriate for organs such as the prostate because of gain and loss of blood and other fluids as well as the presence of a collapsible urethra.

Boundary conditions for each FEA simulation were determined as follows: First, the displacement at each mesh node on the surface of the pelvis was fixed to zero for all simulations. Second, the size and 3D motion of the TRUS probe were specified in terms of the sheath diameter and its motion with respect to a local 3D co-ordinate system, defined from the initial reference position (see Fig. 3). The boundary conditions and ranges used for the material properties are summarised in Table 1. Further discussion on setting appropriate boundary conditions for this problem and on the choice of material properties can be found in Hu et al. (2008a,b).

As illustrated in Fig. 3, the assumed default orientation of the TRUS probe in the lithotomy position is defined by the z-axis of the local co-ordinate system. This axis was orientated at 15° to the cranial-caudal axis in the sagittal plane of the MR image with the patient in the supine position. This value was based on the average angle measured over the MR images used in the study.

Five hundred FEA simulations were performed to provide training data for the statistical model described in the next section. For each simulation, the material properties and boundary conditions were set using values randomly sampled from the ranges given in Table 1. Node displacements were computed using a fast, non-linear FE solver, implemented to enable parallel computations using a graphics processing unit (GPU) (Taylor et al., 2008). A recently developed four-node formulation was adopted to overcome the volumetric locking problem (Bonet and Burton, 1998; Joldes et al., 2009). Using this method, the time taken to perform 500 simulations for each case was approximately 140 min.

2.1.2. Statistical motion modelling

The mesh nodes are first re-sampled from the spherical harmonic surface of the prostate gland with a predefined density. Point correspondence between the deformed prostate models is defined explicitly by the mesh nodes. Therefore, following rigid alignment of the training models, PCA may be applied directly to the 3D displacements of the mesh nodes as follows: If the number of simulated gland deformations in the training dataset is denoted by M ($M = 500$ for this study), then, for each simulation, the x -, y -, and z -components of the calculated displacement of each of N nodes of the prostate gland mesh are combined into a $3N \times 1$ vector,

Table 1

Summary of the boundary conditions and material properties used for the FEA simulations.

Description	Parameter(s)	Range	Reference value(s)	DOF
Probe initial radius	R_0	$[R_0, 1.5R_0]^a$	R_0	1
Probe initial position	T_{0x}, T_{0y}, T_{0z}	$[-5, 5]$ mm	Local coordinates ^b	3
Probe initial orientation	$\theta_{0x}, \theta_{0y}, \theta_{0z}$	$[-10, 10]^\circ$	Local coordinates	3
Probe end radius	R_1	$[R_0, 1.5R_0]$	R_0	1
Probe end position	T_{1x}, T_{1y}, T_{1z}	$[-10, 10]$ mm	Local coordinates	3
Probe end orientation	$\theta_{1x}, \theta_{1y}, \theta_{1z}$	$[-10, 10]^\circ$	Local coordinates	3
Shear modulus	G_1, G_2, G_3, G_4^c	$[3.36, 76.9]$ kPa	–	4
Bulk modulus	K_1, K_2, K_3, K_4^c	$[8.33, 3.33 \times 10^3]$ kPa	–	4

^a R_0 denotes the radius of the TRUS probe used for surgical guidance.

^b Local coordinates are defined by rotating MR coordinates by 15° in sagittal plane and using mid-point of anus as the origin, as illustrated in Fig. 3.

^c The subscripts 1–4 correspond to the prostate central zone (1), peripheral zone (2), the rectal wall (3), and the surrounding tissue (4), respectively.

$$\mathbf{d} = [\delta_{x_1}, \delta_{y_1}, \delta_{z_1}, \delta_{x_2}, \delta_{y_2}, \delta_{z_2}, \dots, \delta_{x_N}, \delta_{y_N}, \delta_{z_N}]^T, \quad (1)$$

where $[\delta_{x_i}, \delta_{y_i}, \delta_{z_i}]^T$ is the displacement vector (following rigid alignment) for the i th node with the co-ordinates (before deformation), (x_i, y_i, z_i) . The vector \mathbf{d} describes the predicted motion of the prostate gland for a particular set of material properties and boundary conditions corresponding to a particular pose of the TRUS probe. A statistical model is formed by computing the modes of variation of \mathbf{d} over the training data using PCA (Cootes et al., 1995). Now, if vector \mathbf{m}_0 contains the 3D coordinates of the nodes of the ‘undeformed’ FE model derived from the MR image, i.e.

$$\mathbf{m}_0 = [x_1, y_1, z_1, x_2, y_2, z_2, \dots, x_N, y_N, z_N]^T, \quad (2)$$

then a deformed gland is defined by vector \mathbf{m} , given by

$$\mathbf{m} = \mathbf{m}_0 + \bar{\mathbf{d}} + \sum_{i=1}^L c_i \mathbf{e}_i, \quad (3)$$

where $\bar{\mathbf{d}}$ is the mean node displacement vector, \mathbf{e}_i is the i th eigenvector of the covariance matrix of the set of training vectors, $\{\mathbf{d}_1, \mathbf{d}_2, \dots, \mathbf{d}_M\}$, and c_i is a scalar weight, which determines the deformed shape of the gland. Eq. (3) models both shape variation and motion, based on the statistics of the training data. Models generating in this way are referred to hereon in as a statistical motion model (SMM). The value of L ($L \leq M$) was chosen so that the SMM covered >99% of variance in the training data. Examples of the shape changes corresponding to changing the weights of the first three principal modes of the shape variation are illustrated in Fig. 4.

To verify the accuracy of a linear SMM generated using PCA, the model generalisation ability (Styner et al., 2003) – i.e. the ability of a model to represent the unseen test data – was calculated for each SMM using the following leave-one-out method: First, for each patient, an SMM is built using 499 training datasets and fitted to the remaining test dataset by computing the least-squares fit of the prostate surface node points of the model to the surface of the test dataset. This process is then repeated 500 times with a different (test) dataset left-out each time. The generalisation ability was defined as the average of the RMS node-to-node distances (across the prostate volume) between the deformed SMM and the test dataset.

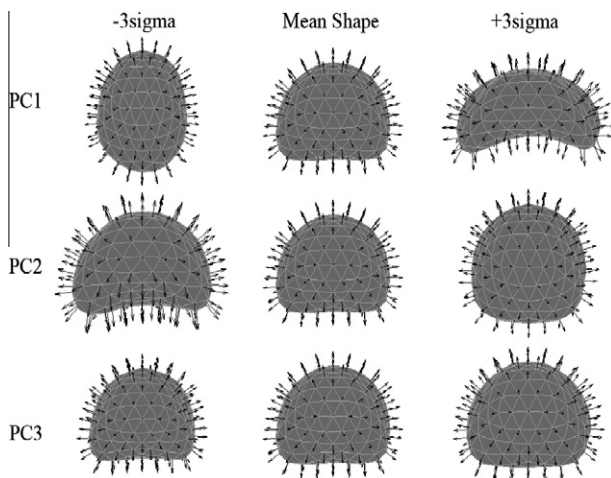


Fig. 4. Changes in the shape of the first three modes of variation (PC1, PC2 and PC3) of a prostate SMM as a result of independently varying the weights corresponding to the first three principal components. The normal vectors at the nodes of the triangulated surfaces, used in the registration scheme, are indicated by arrows ('sigma' is the standard deviation for an individual mode).

2.2. Ultrasound surface feature detection

A relatively well-defined common feature in MR and TRUS images of the prostate gland is the capsule surface. In the registration algorithm proposed here, vector representations of this surface, computed independently from the MR-derived deformable model and the 3D TRUS image, are used to drive a model-to-image registration scheme in which the directional alignment between these vectors is maximised. In this formulation, a set of registration parameters, comprising rigid-body parameters and shape parameters defined by $\{c_1, c_2, \dots, c_L\}$, uniquely define the surface normal vector field, $\mathbf{u}(\mathbf{x})$, where \mathbf{u} is a 3D vector function that defines the surface normal at a particular point in the model space with 3D position vector, \mathbf{x} . By definition, $\mathbf{u} = \mathbf{0}$ at all points not lying on the model surface. In the present work, surface normal vectors were computed for each instance of the gland model at the nodes of the model's triangulated surface mesh.

A surface normal vector field, $\mathbf{v}(\mathbf{y})$, can be defined for the image in a similar way, where \mathbf{y} is a 3D position vector that defines a point in image space. In order to estimate \mathbf{v} , a multiscale filtering technique based on second-order Gaussian derivatives was employed. In this method, the Hessian is first computed at each voxel for a particular scale of the Gaussian derivative operator. The relative magnitudes of the eigenvalues of the Hessian are then used to classify the local structure, which can then be used to enhance blob-, tubular- or sheet-like features in an image (Frangi et al., 1998). In this work, an extension of the sheet-like enhancement filter proposed by Descoteaux et al. (2006) was developed to compensate for the non-uniform US image intensity characteristics found at the capsule boundaries due to artefacts arising from the variable angle between the true surface normal at the boundary and the US beam path. In particular, this effect is responsible for visible differences in the low boundary intensity on the lateral sides of the prostate gland compared to those on the inferior and superior sides of the gland.

In the original formulation described in Descoteaux et al. (2006), the filter response, f_{sheet} , is given by:

$$f_{\text{sheet}}(x, y, z) = \exp\left(-\frac{(R_1)^2}{2\alpha^2}\right) \left(1 - \exp\left(-\frac{(R_2)^2}{2\beta^2}\right)\right) \left(1 - \exp\left(-\frac{(R_3)^2}{2\gamma^2}\right)\right), \quad (4)$$

where λ_1, λ_2 and λ_3 are the ordered eigenvalues of the Hessian computed at point (x, y, z) ($|\lambda_1| \leq |\lambda_2| \leq |\lambda_3|$), $R_1 = |\lambda_2/\lambda_3|$, $R_2 = |2|\lambda_3| - |\lambda_2| - |\lambda_1|$ and $R_3 = (\lambda_1^2 + \lambda_2^2 + \lambda_3^2)^{0.5}$. For the TRUS volumes acquired for this study, the filter response was found to be insensitive to the scalar parameters, α, β and γ , and therefore these were set to the constant values $\alpha = \beta = 0.5$, and $\gamma = \max_{x,y,z}(R_3)$, as suggested in Descoteaux et al. (2006). For simplicity, f_{sheet} was computed for a single scale. A value of 1 mm for the width, σ , (in all directions) of the Gaussian kernel used to compute the Hessian was found to enhance the capsule well.

In order to take the direction of the US beam into account, we propose the modified filter as follows:

$$f_{\text{sheet}}^* = (\mathbf{n}_3^T \mathbf{b})^2 f_{\text{sheet}}, \quad (5)$$

where \mathbf{b} is the 3D vector that defines the radial direction of TRUS beam and \mathbf{n}_3 is the eigenvector corresponding to the largest eigenvalue (λ_3) of the Hessian, which is approximately aligned with the surface normal at the capsule boundary. Therefore, when the direction of the US beam is approximately perpendicular to the surface normal, the sensitivity of the feature vector field to noise is significantly reduced, as illustrated in Fig. 5.

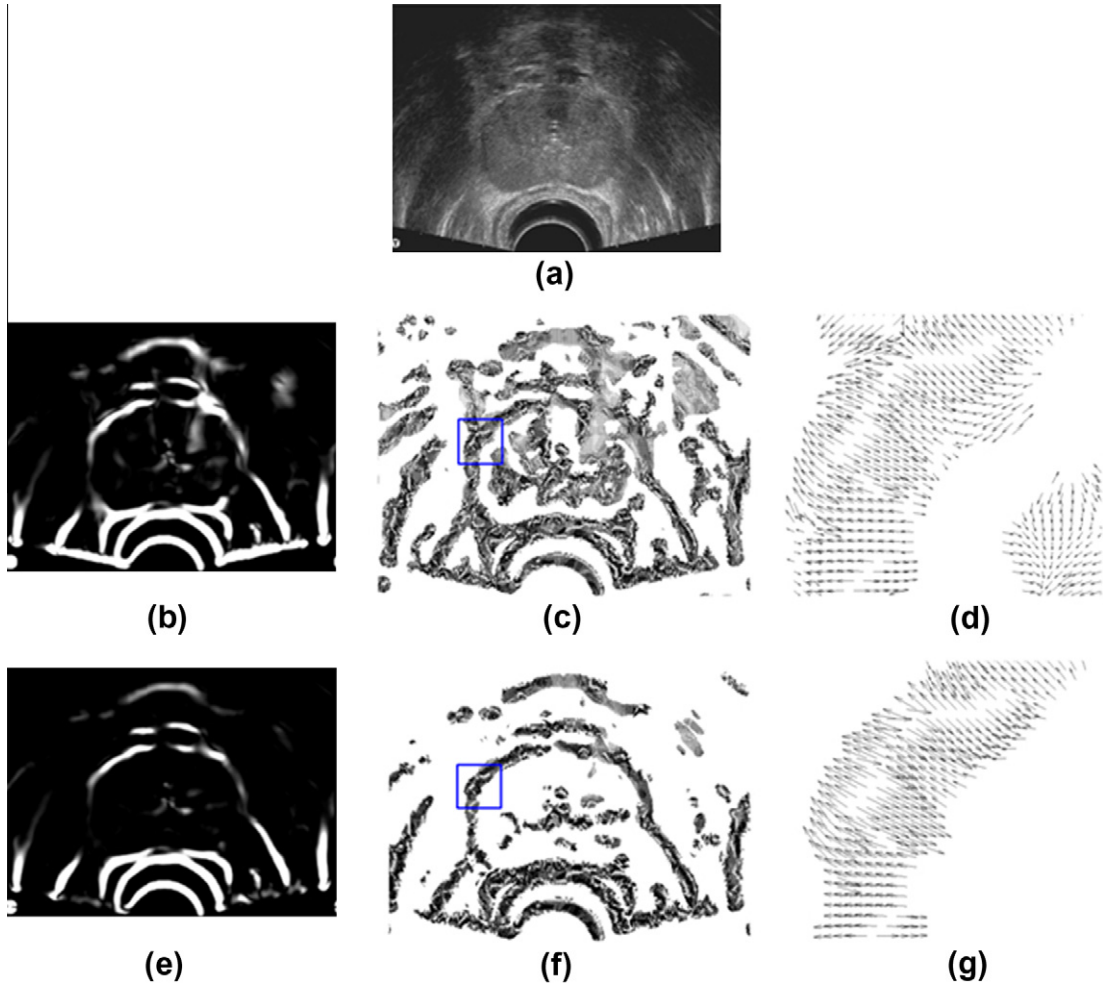


Fig. 5. Example of the surface normal vector field estimated from a 3D TRUS image using the method described in Section 2.2. (a) A transverse slice through the TRUS volume. Images (b) and (e) show the corresponding slice after applying the filter, f_{sheet} and f_{sheet}^* , defined in Eqs. (4) and (5), respectively. Images (c) and (f) show the vector field, v , extracted using these filters, and (d) and (g) show zoomed-in views of the regions indicated in (c) and (f). From inspection of (f), it can be seen that the TRUS beam compensation integrated in f_{sheet}^* results in a significant reduction in noise compared with (c).

Considering only filter responses within a predefined window, the final surface normal vector field is given by:

$$\mathbf{v}(x, y, z) = \begin{cases} \mathbf{n}_3(x, y, z), & \text{if } a \leq f_{\text{sheet}}^*(x, y, z) \leq b \text{ and } \lambda_3 > 0 \\ \mathbf{0}, & \text{otherwise} \end{cases} \quad (6)$$

where the upper and lower limits of the window within which the filter response is considered to be significant are specified by scalars a and b , respectively. An example of the vector field \mathbf{v} computed for a TRUS volume is shown in Fig. 5.

2.3. Surface noise model

To ensure that the registration scheme proposed here is robust to noise in the estimated surface normal vector field, \mathbf{v} , an approach similar to that described by Staib and Duncan (1992) is adopted, since the model-to-image registration problem is equivalent to the boundary finding problem. In the framework proposed by Staib and Duncan (1992), an image-extracted feature, such as the surface normal vector field in the context of this paper, may be considered to be a noise-corrupted version of the corresponding feature determined from a model. Hence, for the present problem, \mathbf{v} may be assumed to be a noise-corrupted version of the surface normal vector field computed for the deformable model \mathbf{m} , defined in Eq. (3).

Now, the conditional probability that a surface normal vector $\mathbf{v} = \mathbf{v}_i$ is measured at the voxel i with co-ordinates $\mathbf{y} = \mathbf{y}_i = (x_i, y_i, z_i)$, $i \in \Omega_{\text{image}}$, given a particular SMM instance, defined by \mathbf{m} , can be expressed as a probability mixture model as follows:

$$f_N(\mathbf{y}_i, \mathbf{v}_i | \mathbf{m}) = \sum_{j \in \Omega_{\text{model}}} h_j f_G(\mathbf{y}_i; \mathbf{x}_j) f_W(\mathbf{v}_i; \mathbf{u}_j), \quad (7)$$

where j is an index to a point in the model space, with co-ordinates $\mathbf{x} = \mathbf{x}_j = (x_j, y_j, z_j)$, $j \in \Omega_{\text{model}}$; h_j is a scalar parameter, which satisfies $\sum_j h_j = 1$; and f_G and f_W are probability density functions that describe the Gaussian and bipolar Watson distribution (Watson, 1983), respectively. Explicitly, f_G and f_W are defined as follows:

$$f_G(\mathbf{y}_i; \mathbf{x}_j) = ((2\pi)^{1.5} |\Sigma_j|^{0.5})^{-1} \exp\left(-\frac{1}{2} (\mathbf{x}_j - \mathbf{y}_i)^T \Sigma_j^{-1} (\mathbf{x}_j - \mathbf{y}_i)\right), \quad (8)$$

and

$$f_W(\mathbf{v}_i; \mathbf{u}_j) = C(k) \exp(k(\mathbf{u}_j^T \mathbf{v}_i)^2) = C(k) \exp(k \cos^2 \theta). \quad (9)$$

In Eq. (8) a special class of anisotropic Gaussian with two parameters is used where the covariance matrix, Σ_j , is defined by a set of orthogonal vectors, $\{\mathbf{w}_1, \mathbf{w}_2, \mathbf{w}_3\}$, such that

$$\Sigma_j = \sum_{d=1}^3 \rho_d \mathbf{w}_d \mathbf{w}_d^T, \quad (10)$$

where $\mathbf{w}_1 = \mathbf{u}_j$ and \mathbf{w}_d , $1 \leq d \leq 3$, represent the orientations of the ellipsoid surface of constant probability density. The two independent parameters, ρ_1 and ρ_2 ($=\rho_3$), govern the extent of the “capture range” of the registration algorithm in the directions normal and tangential to the model surface, respectively. In the experiments described in this study, $\rho_1 = 2\rho_2$.

In Eq. (9), k is a scalar concentration parameter, which is varied depending on the level of noise in \mathbf{v} and is set to a small value ($0.1 < k < 0.5$) in order to weaken the contribution from strong local matches. In 3D, the normalising constant, $C(k)$, is defined by setting the integral of f_W over a sphere to unity, leading to (Schwartzman et al., 2005):

$$C(k) = \left(2\pi \int_0^1 e^{kt^2} \cdot dt \right)^{-1}. \quad (11)$$

In practice, $C(k)$ can be computed by recursive integration. Lastly, the variable θ in Eq. (9) is the angle between the surface normal vector, computed at point j on the model surface, (\mathbf{u}_j) and the estimated normal vector, computed at voxel i in the image (\mathbf{v}_i).

2.4. Registration scheme

The purpose of the registration algorithm is to find the optimal registration parameters which maximise the joint probability of the noise function, f_N (Eq. (7)), given a particular model shape (specified by the shape parameters of the SMM) and pose (specified by the parameters of a rigid-body transformation). Therefore, assuming that the noise values at different voxels are independent, the following log-likelihood function is a suitable objective function for efficient numerical optimisation using the expectation maximisation (EM) algorithm (Dempster et al., 1977):

$$\begin{aligned} f_{obj} &= \log(L(\mathbf{m}|\mathbf{I})) = \log \prod_{i \in \Omega_{\text{image}}} P(\mathbf{I}|\mathbf{m}) = \log \prod_{i \in \Omega_{\text{image}}} f_N(\mathbf{y}_i, \mathbf{v}_i|\mathbf{m}) \\ &= \sum_{i \in \Omega_{\text{image}}} \log \sum_{j \in \Omega_{\text{model}}} h_j f_G(\mathbf{y}_i; \mathbf{x}_j) f_W(\mathbf{v}_i; \mathbf{u}_j) \end{aligned} \quad (12)$$

where \mathbf{I} is a vector that describes the surface normal features derived from the TRUS volume. A modified version of the standard EM algorithm was implemented using Matlab (The Mathworks Inc., Natick, MA, USA), which iteratively updates the registration parameters in order to maximise Eq. (12). Further details are provided in Appendix A.

The user-defined parameters in the registration scheme are the filter parameters, a and b , and the similarity measure parameters, ρ_1 and k . Values for a and b were found by assessing the histograms of the filter responses on a case by case basis and manually setting the thresholds such that outlier features in the filtered image with low and high intensities were eliminated. These parameters were tuned for each of the TRUS scanners used in this study and remained fixed in the registration experiments. Excluding 10–30% of the lowest and highest intensities was found to produce visually optimal filtered images in which the gland surface was clearly enhanced.

Parameters k and ρ_1 were set to 0.1 and 3 mm, respectively. The result of the registration algorithm was found to be insensitive to the k for $0.1 < k < 0.5$ and setting $k \ll 1$ was found to significantly reduce the influence of strong boundaries of the bladder, rectum and pubic arch (sometimes visible in the TRUS images) by weighting the similarity measure in favour of surface normal vectors that are not perfectly aligned. Similarly, the algorithm is relatively insensitive to the value of ρ_1 . This parameter determines the local search range for the algorithm and was set to the average distance between surface node points.

2.5. Patient validation

2.5.1. Image acquisition

All patient data used in this study was obtained from patients recruited to clinical research studies carried out at University College London Hospital. These studies were approved by the local research ethics committee, and all patients gave informed, written consent to participate. Data from eight patients with prostate cancer were used to validate the registration method.

T2-weighted MR images were acquired on all the patients using a Siemens 1.5 T MR scanner and a pelvic phased-array coil with the patients in the supine position. The 3D MR volumes had an in-plane resolution of between 0.3 and 0.4 mm/pixel with a slice thickness of 3.0 mm. MR scans were performed prior to template-guided, transperineal needle biopsy procedures (seven patients) or, for one case, a HIFU ablation as a treatment for localised prostate cancer.

All procedures were performed under general anaesthesia and 3D TRUS images of the gland were acquired at the beginning of the procedure with the patient placed in the lithotomy position. For the biopsy patients, transverse B-mode images were captured at 2 mm intervals using a B-K ProFocus scanner (B-K Medical Ltd., Berkshire, UK) and bi-planar side-firing transrectal probe (5–7.5 MHz B-K 8658T transducer) attached to a mechanical stepping device (Tayman Medical Inc., MO, USA). For each patient, the TRUS volume comprises a set of parallel B-mode slices. Each image was stored on the scanner after using the stepper to translate the probe along the rectum before being transferred to a PC for offline analysis. The TRUS volume for the patient undergoing HIFU therapy was obtained automatically before treatment commenced using a Sonablate 500 HIFU system (Focus Surgery, Inc., Indianapolis, IN, USA).

2.5.2. Data processing

Following manual segmentation of the MR images and FE mesh generation, as outlined in Section 2.1.1, 500 biomechanical simulations were performed for each case using a C++ implementation of a non-linear finite element solver (Taylor et al., 2008). The simulations were executed on a desktop PC with a 2.33 GHz Intel® Core™ dual CPU processor and 3 GB of RAM installed with a 256 MB NVIDIA® GeForce™ 8600 GT GPU. Each simulation took on average 16 s to compute the deformation for a FE model with approximately 45,000 elements.

The deformed FE models resulting from these simulations were then used to build a patient-specific SMM for each case, as described in Section 2.1.2. The number of modes used in each SMM was determined by finding the value of L (Eq. (3)) that resulted in at least 99% of the variance in the training data being described by the model. For the purposes of registration, a high-density, triangulated surface mesh was also created for each SMM.

Each set of TRUS images was reconstructed into a volume with an isotropic voxel dimension of 1 mm. An implementation of the sheetness filter (Eqs. (4) and (5)) was coded using Matlab. In this algorithm, the Hessian was computed using a frequency domain approach based on the fast Fourier transform.

2.5.3. Evaluation of registration accuracy

To evaluate the performance of the proposed registration method, 100 MR–TRUS registrations were performed for each of the eight patients. The model-to-image registration algorithm was implemented in Matlab, and a quick and simple initialisation procedure was adopted in which one point at the apex and base of the gland were identified manually in the TRUS volume. The initial pose of the SMM with respect to the TRUS volume was then calculated by finding the least-squares alignment of the model and TRUS apex–base axes with the constraint that the model cannot rotate

about the apex–base axis. Once registered, a dense displacement field (DDF) was computed from the final instance of the deformable FE mesh by interpolation.

In order to simulate variability in the initialisation base and apex points and to investigate the robustness of the registration algorithm given different model starting positions, a random starting position was set before each registration by adding a random error ≤ 5 mm, drawn from a uniform probability distribution, to each of the x -, y -, and z -components of the original, manually identified apex and base points. The accuracy of each registration was quantified by computing the final root mean square (RMS) target registration error (TRE) between corresponding anatomical landmark points, identified in the MR and TRUS images, following registration. The 3D co-ordinates of landmarks, defined in an MR image, were transformed into TRUS co-ordinates using the DDF.

As a comparison, the same model-based registration framework, with the same parameter settings, was used to rigidly register the original gland surface segmented from MR to the TRUS image, but where the step in which the shape parameters are estimated as omitted. Again, registrations were performed using the same random initialisations as used for the non-rigid registrations, and the TRE was computed by propagating the landmarks using the resulting rigid transformation.

The landmarks used for estimating the TREs were identified manually by a urological surgeon with over 5 years experience in interpreting prostate ultrasound and MR images. A custom written Matlab tool was used for this purpose. For each prostate, the following three landmarks were defined in both the TRUS and MR volumes on three separate occasions: the point in the centre of the urethra as it enters and exits the prostate – i.e. at the base and apex of the gland – and the centrepoin where the ducts of the seminal vesicles emerge from the gland. In addition, the locations of the centres of small cysts and calcifications appearing inside the gland were identified, again on three separate occasions. In general, cysts appear as low-intensity (hypoechoic) features in the TRUS images and high-intensity regions in the MR, whereas calcifications appear with high-intensity (hyperechoic) in the TRUS images and low-intensity in the MR. All landmarks were defined by identifying the image co-ordinates in three orthogonal slices using the Matlab-based tool developed by the Authors. The gold standard position for each landmark was found by averaging the co-ordinates defined on three separate occasions.

For each pair of gold standard landmarks, the TRE was defined as the Euclidean distance between the landmark originally defined in TRUS co-ordinates and the location of the corresponding MR landmark following propagation into the TRUS space. MR images were also warped into the TRUS co-ordinate system using the DDF to allow visual assessment of the MR–TRUS registration.

To estimate the precision of localising individual landmarks, a landmark localisation error (LLE) was computed. For each landmark, the LLE was defined as the RMS distance between the gold standard (i.e. mean) landmark co-ordinates and each of the three landmark co-ordinates defined by the expert observer.

2.5.4. Comparison with a surface-driven registration method

One useful property of an SMM, unlike general-purpose non-rigid (or elastic) transformations, is that it ensures that prostate gland deformations are highly constrained and incorporate prior knowledge on the range of deformations expected during a procedure. This feature is particularly important for robust registration to US images because the low signal-to-noise ratio and artefacts associated with this modality. Alternative transformation models have been proposed, such as the linear-elastic volumetric warping methods used by Bharatha et al. (2001), Haker et al. (2004), and Narayanan et al. (2009). In these studies, a FE model was used directly to compute the image deformation field following a surface-based registration, which sets the boundary conditions at the surface of the gland. To compare our approach with this method, we evaluated the accuracy of an alternative elastic registration algorithm in which the non-linear FE solver was used to determine the deformation field given surface displacements found by registering the MR-derived gland surface to the surface segmented manually from the TRUS image.

In this experiment, the prostate gland surface of the FE mesh used to build the SMM was chosen as the source surface. This was then registered to a dense set of TRUS target surface points using the coherent point drift (CPD) algorithm (Myronenko et al., 2006; Myronenko and Song, 2010). G and K for the interior of the gland were set to 40.1 kPa and 1.67 GPa, respectively. These values are the average values of the corresponding ranges shown in Table 1. As with the SMM-based method, the solution provides a volumetric displacement field across the gland, which is used to propagate landmarks. As before, TREs were computed by measuring the distance between each propagated landmark and the corresponding landmark identified in the target TRUS image.

3. Results

The mean \pm SD generalisation ability, defined in Section 2 and calculated over all SMMs generated for eight patient datasets, was 0.30 ± 0.09 mm. This low value indicates that a linear SMM was able to capture the simulated prostate motion predicted by the FE model adopted in this study.

A summary of the initial and final landmark-based TREs for each patient case is given in Table 2. The initial TREs were calculated

Table 2

TREs computed for registrations using the automatic rigid and deformable SMM-based method (Cases 1–7 were template-guided biopsies and Case 8 was a HIFU ablation) The LLE and contributions of the magnitude of the rigid and non-rigid components of the non-rigid transformation (expressed as the AND – see text) resulting from the deformable registrations are also given for each case.

Case no.	L	No. of landmarks	Initial RMS TRE (mm)		Final RMS TRE (mm) (rigid)		Final RMS TRE (mm) (deformable)		Deformation (RMS AND) (mm)		LLE mean \pm SD (mm)	
			Median	95% CL	Median	95% CL	Median	95% CL	Rigid	Non-rigid	MR	US
1	13	5	9.42	11.39	9.47	12.13	2.68	7.21	8.23	3.04	1.53 \pm 1.23	1.90 \pm 2.17
2	11	3	14.52	17.43	4.47	7.73	3.19	9.62	12.54	0.68	1.02 \pm 0.75	1.62 \pm 1.99
3	11	3	6.29	9.62	3.14	6.09	1.69	5.38	6.00	1.73	2.99 \pm 1.21	1.25 \pm 0.43
4	11	4	6.24	9.42	3.20	6.27	1.56	5.21	6.56	1.83	3.15 \pm 1.96	1.84 \pm 1.93
5	10	5	9.32	11.14	9.54	12.33	2.60	6.84	3.29	2.96	4.63 \pm 2.94	1.89 \pm 2.36
6	12	3	5.86	8.75	2.81	5.22	1.58	4.65	4.41	2.44	1.94 \pm 1.35	1.39 \pm 0.99
7	11	4	8.84	11.65	10.38	13.72	2.92	7.49	4.01	2.84	1.20 \pm 0.63	1.16 \pm 0.68
8	10	4	6.15	8.98	3.09	5.74	1.49	4.66	7.08	2.07	1.71 \pm 1.16	0.89 \pm 0.55
All	–	31	8.13	15.02	5.11	12.05	2.40	6.19	7.32	2.19	2.35 \pm 1.92	1.53 \pm 1.52

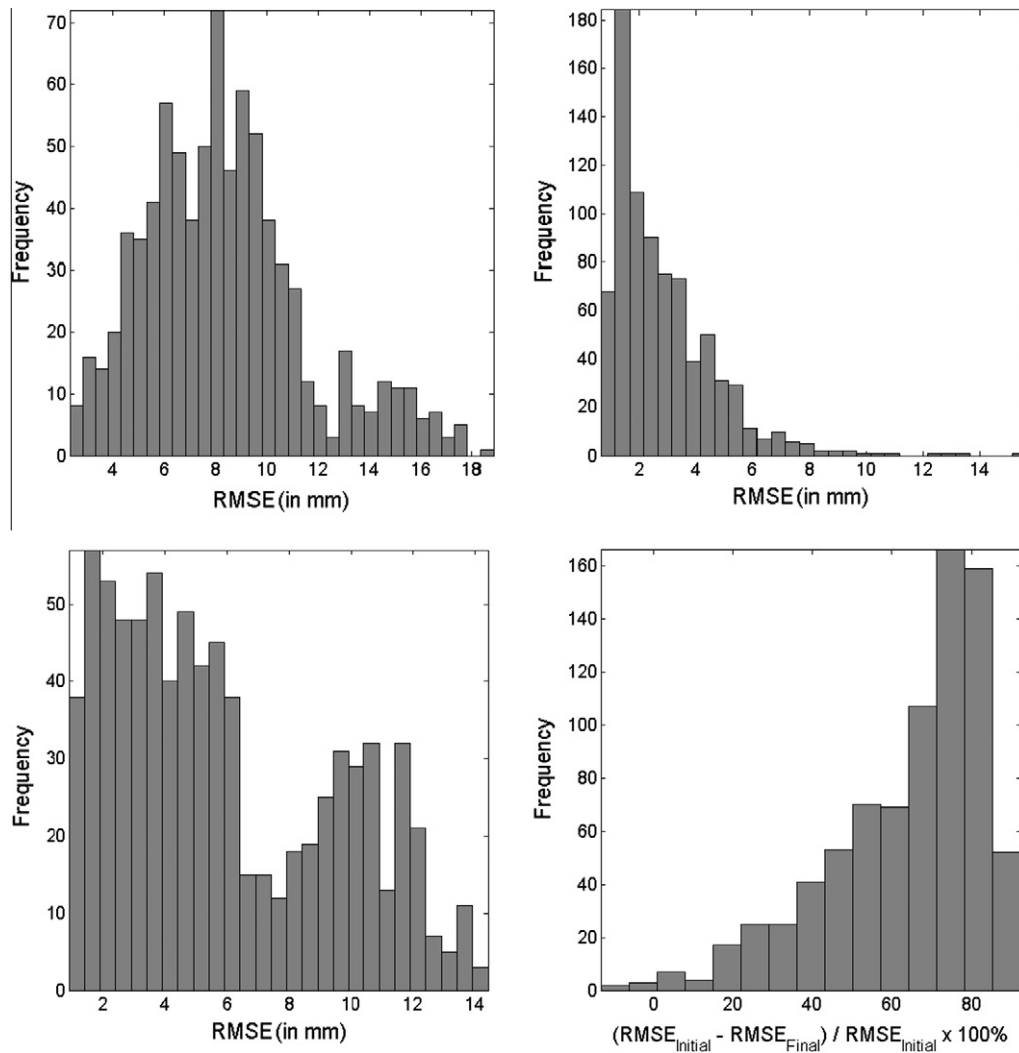


Fig. 6. Histograms of the RMS TRE calculated before and after 800 registrations of MR-derived SMM and TRUS images (100 registrations per case). Top left: the initial TRE after manual rigid initialisation; Top right: the final TRE following registration using the automatic deformable SMM-based method; Bottom left: final TRE following automatic rigid registration of the SMM without allowing it to deform; Bottom right: relative change in TRE, expressed as a percentage reduction from initial to final TRE using the deformable registration method.

Table 3
TREs and LLEs calculated for registrations using the automatic SMM-based method, grouped according to the type of landmark.

Landmark	No. of landmarks	Initial RMS TRE (mm)		Final RMS TRE (mm)		LLE mean \pm SD (mm)	
		Median	95% CL	Median	95% CL	MR	US
Apex	8	9.88	11.80	3.62	6.09	2.12 \pm 1.83	2.72 \pm 2.00
Base	8	10.52	12.77	3.14	6.59	2.13 \pm 0.98	1.27 \pm 0.96
JGSV ^a	8	7.77	10.35	3.01	5.49	2.69 \pm 1.93	1.59 \pm 1.38
Cysts/calcifications	7	5.83	7.22	1.92	3.74	2.49 \pm 2.97	0.39 \pm 0.25

^a JGSV denotes the junction between the gland and the seminal vesicles as described in Section 2.5.3.

following initialisation by rigid alignment of the base-apex axes, as described in Section 2.5.3. The histogram of the initial and final RMS TREs are shown in Fig. 6.

The overall median RMS TRE was 2.40 mm across the eight patient cases using the deformable SMM-based method. The magnitudes of rigid and non-rigid components of the registration transformation were quantified by separately calculating the absolute node displacement (AND) for FE mesh nodes locations over the entire gland due to the rigid and shape transformations respectively. The results for each patient are given in Table 2.

A histogram of the final RMS TREs resulting from the rigid registrations is shown in Fig. 6; a summary of the numerical TREs for each case is given in Table 2. Inspection of Fig. 6 and Table 2 reveals that a significant improvement in TRE was achieved by including the deformable component in the registrations, especially for cases 1, 5, and 7. Overall, the median RMS TRE was improved from 5.11 mm, obtained using rigid registration, to 2.40 mm, obtained using the proposed deformable registration scheme. This finding highlights the importance taking into account deformation between MR and TRUS imaging to achieve the highest accuracy.

Table 4

TREs and LLEs calculated for surface-driven registrations.

Case no.	Final RMS TRE (mm)		MR–TRUS surface distance (mm)
	Median	95% CL	
1	3.62	4.33	0.68
2	2.25	4.27	0.57
3	5.71	7.04	0.59
4	5.76	7.50	0.71
5	10.03	10.55	0.61
6	8.44	9.33	0.53
7	3.48	4.59	0.52
8	6.51	8.67	0.57
All	5.45	9.95	0.60

Table 5

TREs calculated for surface-driven registrations, grouped according to the type of landmark.

Landmark	Final RMS TRE (mm)	
	Median	95% CL
Apex	5.72	7.55
Base	6.68	7.62
JGSV	4.59	5.81
Cysts/calculifications	7.77	9.22

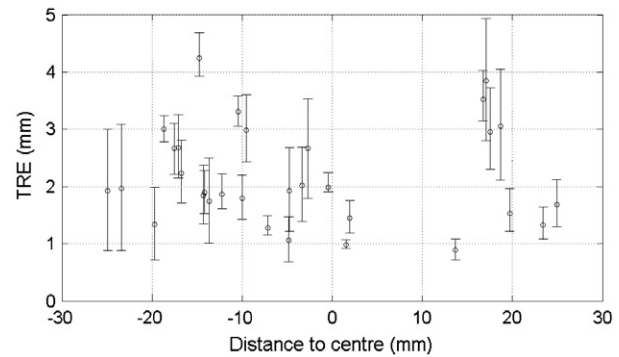
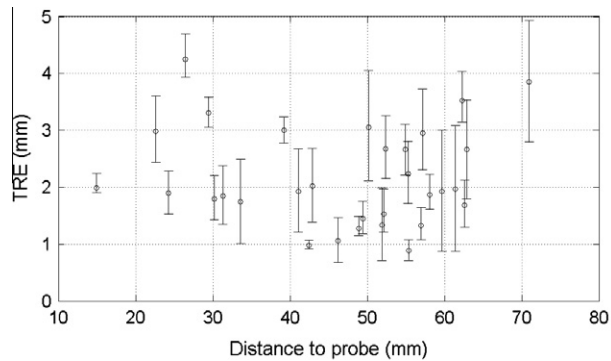


Fig. 7. Plots of the spatial distribution of TRE: Left, the TRE is plotted against the perpendicular distance from the TRUS probe axis in the anterior–posterior direction; right, the TRE is plotted against the perpendicular distance from the mid-gland transverse plane (positive distances are near to the apex and negative distances are near to the base). In both cases, the errors are plotted as a median (circle) of 100 registration trials for eight patients. The error bars indicate the 5th and 95th percentiles.

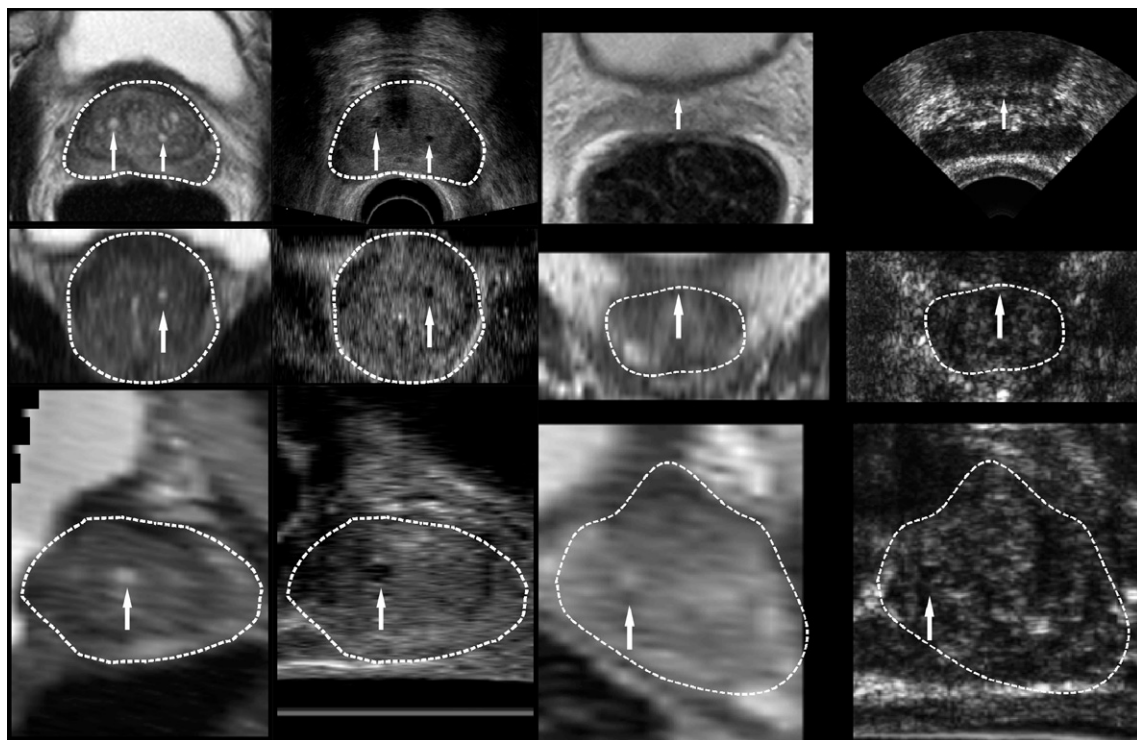


Fig. 8. Examples of transverse (top row), coronal (middle row) and sagittal (bottom row) views through registered MR (left column) and TRUS (right column) volumes for Case 1 (left; biopsy case) and Case 8 (right; HIFU case). The MR volume has been warped using the dense displacement field calculated from the FE model. The arrows indicate landmarks which were well aligned following registration.

The TREs computed for the surface-driven registration method are given in Table 4 and 5. The median RMS TRE in this case was 5.4 mm. The result for this method compares with a mean TRE of 3.06 ± 1.41 for MR-to-TRUS registration of a phantom prostate

reported by Narayanan et al. (2009). Comparing with the SMM-based method, although the surface fit was relatively good – the RMS point-to-surface distance ranged from 0.52 to 0.71 mm – the TRE was approximately 45% higher than the

SMM-based method. It is also important to note that this method requires segmentation of the target TRUS surface and is dependent on the accuracy of this segmentation. In contrast, segmentation of the capsule in TRUS images is not required by the automatic model-to-image technique proposed in this paper.

Inspection of the LLEs given in Tables 2 and 3 reveals no obvious relationship between these two measures, but the LLE was found to be larger for MR images compared with TRUS images. This may be attributed to the lower resolution of the MR images, particularly between slices, which introduces greater uncertainty in localising landmarks.

The spatial distribution of the registration error has important implications for the clinical application of MR–TRUS registration, since the peripheral zone of the prostate gland is known to be the most common site harbouring cancer (McNeal et al., 1988). To investigate the spatial distribution of the TREs within the prostate, the TREs were plotted (i) versus the perpendicular distance from the TRUS probe axis in anterior–posterior direction, and (ii) versus the perpendicular distance from the mid-gland transverse plane. The results, shown in Fig. 7, reveal no obvious relationship between the TRE and the distance from the probe axis, suggesting that the errors independent of spatial location. However, inspection of the second plot in Fig. 7 indicates that the TRE was found to be significantly larger near to the apex of the gland. We attribute this observation to the difficulty associated with accurately segmenting the prostate in the transverse MR slices at the ends of the gland, and in identifying the apex landmark point in the TRUS images, as suggested by the relatively high LLE computed for this landmark (see Table 3). Fig. 8 illustrates the results of warping MR and target TRUS images using the DDF computed from two example registrations.

4. Discussion

In this paper, we have introduced a new method for automatic non-rigid registration of MR and TRUS images of the prostate in which the problem is posed in a model-to-image framework. Underlying the method is a novel probabilistic formulation of the feature-based registration problem where surface normal vectors are chosen as the feature of interest. We propose a new method for estimating these vectors from a 3D US image using a second-order Gaussian filtering approach, which has significantly reduced sensitivity to noise compared to a conventional filtering approach by taking into account the direction of the US beam path. A modified EM scheme is also proposed which enables a fast and robust registration given a starting estimate for the rigid-body component of the registration transformation provided by a simple initialisation procedure.

The registration errors presented in this paper result compare well with errors recently reported for non-rigid MR–MR registration by Oguro et al. (2009). In their study, the mean fiducial registration error (FRE) – equivalent to the TRE reported here – was 2.8 ± 1.8 mm after registering preoperative 1.5 T MR images of prostates of patients in the supine position to 0.5 T interventional MR images acquired during MR-guided brachytherapy with the patients in the lithotomy position. An intensity-based B-spline registration algorithm was used for this purpose, but it is difficult to see how this algorithm could be easily applied to TRUS–MR image registration given the substantial differences in intensity characteristics between the modalities.

The potential for misclassification of clinically significant prostate cancer is a major problem with conventional transrectal biopsy schemes, and 5 mm-grid-based saturation schemes have been proposed to improve the detection of significant disease that would otherwise be missed by conventional methods

(Epstein et al., 2005; Scattoni et al., 2007). MR-targeted biopsy offers an alternative approach with the potential benefit that the number of biopsy samples required to establish an accurate diagnosis is much lower than saturation schemes. The practical level of targeting accuracy necessary to make this approach clinically useful is as yet unknown and will depend on the tumour localisation accuracy of the MR imaging technique employed.

Adopting the widely used cutoff of 0.5 cm^3 for clinically significant tumour volume, and assuming that the centre of clinically significant target tumours can be localised with negligible error, negligible needle deflection, and, for simplicity, a spherical and a pathologically homogeneous tumour model, a targeted tumour will be hit when the system targeting error is less than 4.92 mm (equal to the radius of a 0.5 cm^3 sphere). Furthermore, assuming that the targeting error is normally distributed with variance σ^2 in each of the x -, y -, and z -components, the targeting error, defined as the distance between the true centre of the target tumour and a target point calculated by the image guidance system will follow a Maxwell–Boltzmann PDF. Given this distribution, the TRE, expressed as the RMS distance error, is equal to $\sqrt{3}\sigma$ (see Appendix B for the derivation of this result), and, given a particular threshold on the (clinically significant) tumour hit-rate, it is possible to derive the corresponding RMS TRE threshold below which the specified hit-rate will be achieved. For example, if a tumour hit-rate of 90% is set, the corresponding RMS TRE threshold is 3.41 mm (see Appendix B and Fig. 9). Fig. 10 shows a graph of the percentage of registrations meeting a particular hit-rate for detecting a 0.5 cc prostate tumour as a function of the hit-rate. Using this 90% hit-rate threshold, we observe that over 93% of the registrations performed in this study met this criterion.

This calculation provides a crude estimate of system performance in a clinical context. However, in practice, tumours are neither spherical nor homogeneous, and additional sources of errors will be present. How the performance of an MR-targeted biopsy system compares with conventional and saturation schemes under realistic conditions, together with the accuracy required to achieve disease control from ablative interventions, are topics for future investigation.

An important practical feature of our method is the simple two-point initialisation (which provides the initial rigid-body transformation). This step can be carried out quickly and easily in the clinical setting. The registration method was found to be

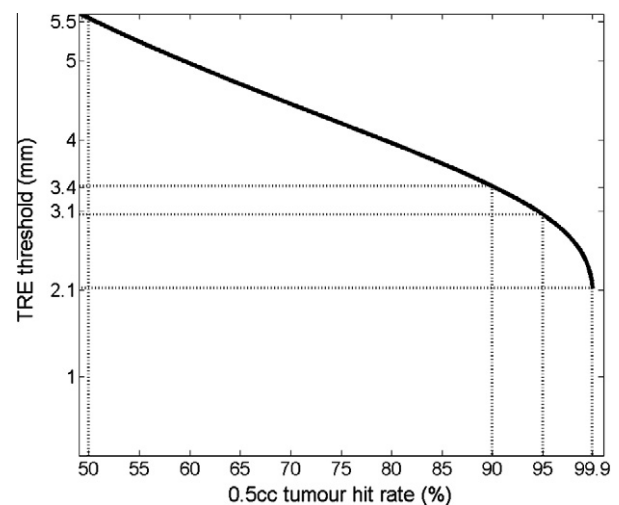


Fig. 9. Plot shows the TRE threshold as a function of the hit-rate.

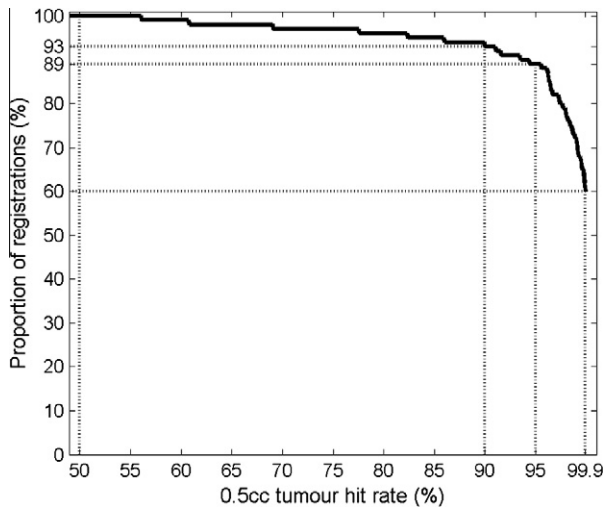


Fig. 10. Plot shows a graph of the percentage of registrations meeting a particular hit-rate for detecting a 0.5 cc prostate tumour as a function of the hit-rate.

robust to different starting positions, simulated by adding a random error to two manually-defined starting points. However, it should be borne in mind that using a fixed level of error in this way for all cases does not result in equivalent initial TREs due to different sizes of prostate gland which means that the effect of introducing a random initialisation error on the initial TRE was greater for smaller glands than for larger glands.

A significant limitation of the model-to-image approach adopted here is the prerequisite for a geometric anatomical model of the organs of interest. Preoperative anatomical models which incorporate a surgical plan are widely used in many other image-guided interventions, such as orthopaedic surgery, since they provide an intuitive and easy-to-interpret representation of anatomy and treatment strategy. Therefore, there are clear advantages to obtaining a geometric model of anatomy since such models are useful for defining precisely a treatment/biopsy plan and for implementing this plan using image guidance. In the present study, a patient-specific FE model based on a segmented MR image was chosen. Once an FE model is obtained, processing to predict deformation is a relatively straightforward task, which can be performed automatically, with little or no user-interaction. However, it is clear that the generation of a model of this kind adds significant time and complexity to the clinical workflow. In the present application, this task is not time-critical since it can be performed at any time between MR imaging and a procedure, which in practice is usually a period of days to weeks. From a clinical workflow perspective, the most significant part of the model generation is the segmentation of the MR image, especially if manual segmentation is employed, as in this study (the FE mesh generation, the FEA simulations, and the SMM generation processes are computationally intensive, but completely automatic). Manual segmentation arguably provides the most accurate data for FE model building and FEA, but requires significant anatomical knowledge, user-interaction and is time-consuming. Consequently, manual MR segmentation may be difficult to justify in some centres, although it is envisaged that such a procedure could be accepted, for instance, as part of a high-accuracy treatment planning protocol for patients undergoing targeted therapy for localised prostate cancer, particularly in a clinical research setting. Nevertheless, alternative, semi- or fully-automatic techniques are highly desirable.

In our experience, the majority of the segmentation time is required to segment the pelvic bone, which has a complex geometry

compared with that of the prostate. We are currently exploring alternative, automatic methods for segmenting the pelvic bone (Thompson et al., 2008), which would significantly reduce the segmentation time. It is also possible that the accurate segmentation of the pelvis is not required since a simplified representation of the pelvic may be sufficient to produce a model that does not have a significant impact on the registration accuracy (Hu et al., 2008a). This is the subject of current research beyond the scope of the present work.

Compared with pelvis segmentation, segmenting the prostate and bladder near to the base of the prostate is less complicated and less time-consuming when performed manually. Nevertheless, this task would benefit from automatic segmentation, for example using the method described by Klein et al. (2008), Pasquier et al. (2007), and Makni et al. (2009). We are currently actively investigating statistical motion modelling techniques similar to those employed in this study to create generic, population-based models of the prostate gland, which could be used to automatically segment MR images using an adaptation of the model-to-image registration algorithm.

In the FE simulations of gland deformation, for simplicity we have not explicitly accounted for a change in shape of the prostate gland that may occur due to a change in patient position between the MR and TRUS imaging sessions. Hirose et al. (2002) comment that a change in gland shape due to the change from the supine to the lithotomy position may be an important factor in the prostate shape change observed in their study, but since supine MR images were acquired using an endorectal MR coil, whilst MR images with the patient in the lithotomy position were acquired with a rectal obturator in place, it is impossible to determine the contribution on the gland shape change of the change in patient position relative to the forces imposed by these devices.

In the present study, we assume that any shape change due to the change in patient position is effectively modelled by considering a significantly wider range of TRUS probe poses than would be encountered in practice in the FE simulations. In this way, changes in the relative orientation of the anal–rectal and prostate (apex–base) axes due to a change in patient position are accounted for since the former governs the angle of insertion of the TRUS probe in the lithotomy position.

However, since the contribution to the total prostate gland deformation of a change from the supine position to the lithotomy position has not been quantified, our assumption that the contribution is negligible is speculative and requires further verification. Such verification was outside the scope of the present study and is the subject of future work.

The computational burden of FEA simulations was reduced significantly by employing a parallelised, GPU-based implementation of the FEA solver, which meant that a single FE simulation could be performed within 20 s. To the best of authors' knowledge, this work is the first to report an image registration method that integrates the high-speed, GPU-based FE modelling with statistical shape modelling techniques to efficiently generate a physically-constrained deformable organ model for registration during image-guided intervention applications. The use of a physically-constrained model has considerable advantages over alternative methods as it leads to a registration that is robust to noise in the target image, but flexible enough to permit significant deformation.

In this work, the FE simulations were limited to predicting prostate motion due to placement of a TRUS probe in the rectum. However, this could be extended to model other situations, such as the removal of an endorectal coil used in some MR imaging protocols, or freehand motion of an end-firing TRUS probe during transrectal biopsy.

Acknowledgements

This work is funded by the UCLH/UCL Comprehensive Biomedical Research Centre grant (Project Grant Ref. 96) and a Royal Academy of Engineering/EPSRC Research Fellowship held by Dr. Dean Barratt. This work was undertaken at UCLH/UCL who received a proportion of funding from the Department of Health's NIHR Biomedical Research Centres funding scheme. The authors would like to thank Philip Batchelor from King's College London and colleagues Tim Carter, Daniel Heanes, Gerard Ridgway and Xiahai Zhuang in the Centre for Medical Image Computing (CMIC) at University College London for helpful ideas and discussions.

Appendix A. EM algorithm

A.1. Objective log-likelihood function

Rewriting Eq. (7), we have:

$$f_{obj} = \sum_{i=1}^I \log \sum_{j=1}^M h_j f_G(\mathbf{y}_i | \mathbf{x}_j) f_W(\mathbf{v}_i | \mathbf{u}_j) \quad (\text{A1})$$

where I is the number of voxel-based features and M is the number of sampled points on the deformable surface model.

A.2. E-step

The posterior probability of the latent variable, also known as membership probability or responsibility, is given by:

$$\gamma_{ij}^m = \frac{h_j^m f_G(\mathbf{y}_i | \mathbf{x}_j^m) f_W(\mathbf{v}_i | \mathbf{u}_j^m)}{\sum_{k=1}^M h_k^m f_G(\mathbf{y}_i | \mathbf{x}_k^m) f_W(\mathbf{v}_i | \mathbf{u}_k^m)} \quad (\text{A2})$$

where the superscript m denotes the estimates in m th step of the EM algorithm ($m = 0$ at the start). Now, the expected complete-data log likelihood is:

$$\begin{aligned} Q^m &= \sum_{j=1}^M \sum_{i=1}^I (\gamma_{ij}^m \cdot \log h_j^m) + \sum_{j=1}^M \sum_{i=1}^I (\gamma_{ij}^m \cdot \log f_G(\mathbf{y}_i | \mathbf{x}_j^m)) \\ &\quad + \sum_{j=1}^M \sum_{i=1}^I (\gamma_{ij}^m \cdot \log f_W(\mathbf{v}_i | \mathbf{u}_j^m)) \\ &= \sum_{j=1}^M \sum_{i=1}^I \left\{ \gamma_{ij}^m \cdot \left[\log(h_j^m) + \log \left(\frac{1}{(2\pi)^{3/2} |\Sigma_j|^{1/2}} \right. \right. \right. \\ &\quad \times \exp \left(-\frac{1}{2} (\mathbf{y}_i - \mathbf{x}_j^m)^T \Sigma_j^{-1} (\mathbf{y}_i - \mathbf{x}_j^m) \right) \Big] \\ &\quad \left. \left. + \log \left(C(\kappa) \exp(\kappa ((\mathbf{u}_j^m)^T \mathbf{v}_i)^2) \right) \right] \right\} \quad (\text{A3}) \end{aligned}$$

A.3. M-step

A.3.1. Surrogate maximum likelihood estimators (MLEs)

As in the standard EM algorithm for a mixture density model (Bilmes, 1997), if we let λ_m denote the Lagrange multiplier due to the constraint $\sum_{j=1}^M h_j = 1$, the updated mixing parameter is calculated by differentiating (A4) with respect to h_j , setting the resulting derivative to zero, and solving as follows:

$$\frac{\partial Q^m}{\partial h_j} = \frac{\partial}{\partial h_j} \left\{ \sum_{i=1}^I \sum_{j=1}^M \gamma_{ij}^m \cdot \log h_j \right\} + \lambda_m \left(\sum_{j=1}^M h_j - 1 \right) = 0 \quad (\text{A4})$$

$$\Rightarrow \sum_{i=1}^I \frac{1}{h_j} \gamma_{ij}^m + \lambda_m = 0 \quad (\text{A5})$$

$$\Rightarrow h_j^{m+1} = \frac{1}{I} \sum_{i=1}^I \gamma_{ij}^m \quad (\text{A6})$$

To update the spatial parameters, we perform the procedure:

$$\frac{\partial Q^m}{\partial \mathbf{x}_j} = \frac{\partial}{\partial \mathbf{x}_j} \left\{ \sum_{i=1}^I \sum_{j=1}^M \gamma_{ij}^m \cdot \left[-\frac{1}{2} (\log |\Sigma_j|) - \frac{1}{2} (\mathbf{y}_i - \mathbf{x}_j)^T \Sigma_j^{-1} (\mathbf{y}_i - \mathbf{x}_j) \right] \right\} = 0 \quad (\text{A7})$$

$$\Rightarrow \sum_{i=1}^I \gamma_{ij}^m \cdot \Sigma_j^{-1} (\mathbf{y}_i - \mathbf{x}_j) = 0 \quad (\text{A8})$$

$$\Rightarrow \hat{\mathbf{x}}_j = \sum_{i=1}^I \gamma_{ij}^m \cdot \mathbf{y}_i / \sum_{i=1}^I \gamma_{ij}^m \quad (\text{A9})$$

To estimate directional parameters subject to the constraint $\mathbf{u}_j^T \mathbf{u}_j = 1$, if we let λ_w denote the Lagrange multiplier due to the normalized vector constraint, we have:

$$\frac{\partial Q^m}{\partial \mathbf{u}_j} = \frac{\partial}{\partial \mathbf{u}_j} \left\{ \sum_{i=1}^I \sum_{j=1}^M \gamma_{ij}^m \cdot \left[\log(C(\kappa)) + \kappa (\mathbf{u}_j^T \mathbf{v}_i)^2 \right] - \lambda_w (\mathbf{u}_j^T \mathbf{u}_j - 1) \right\} = 0 \quad (\text{A10})$$

$$\Rightarrow \sum_{i=1}^I \gamma_{ij}^m \cdot (2\kappa \cdot \mathbf{v}_i \mathbf{v}_i^T \mathbf{u}_j) - 2\lambda_w \mathbf{u}_j = 0 \quad (\text{A11})$$

Now, pre-multiplying by \mathbf{u}_j^T gives

$$\lambda_w = \kappa \sum_{i=1}^I \gamma_{ij}^m \cdot (\mathbf{u}_j^T \mathbf{v}_i \mathbf{v}_i^T \mathbf{u}_j) = 0 \quad (\text{A12})$$

It is shown in Figueiredo and Gomes (2006) that the MLE $\hat{\mathbf{u}}_j$ is the eigenvector associated with the largest eigenvalue of $\sum_{i=1}^I \gamma_{ij}^m \cdot \mathbf{v}_i \mathbf{v}_i^T$:

$$\left(\sum_{i=1}^I \gamma_{ij}^m \cdot \mathbf{v}_i \mathbf{v}_i^T \right) \hat{\mathbf{u}}_j = \hat{w}_j \hat{\mathbf{u}}_j \quad (\text{A13})$$

A.3.2. Registration parameters

After the mixing, spatial and directional MLEs are updated, the registration parameters can be updated using a weighted least-squares scheme, as follows:

$$\begin{aligned} \hat{\theta}_{rigid} &= \arg \min_{\theta_{rigid}} \sum_{j=1}^M h_j^{m+1} (\pi^{-1} \|\hat{\mathbf{x}}_j - T_{rigid}(\mathbf{x}_j^0, \theta_{rigid})\|^2 \\ &\quad + k \|\hat{\mathbf{u}}_j - T_{rigid}(\mathbf{u}_j^0, \theta_{rigid})\|^2) \quad (\text{A14}) \end{aligned}$$

where T_{rigid} is a rigid-body transformation applied to the spatial and directional vectors given the parameter vector, θ_{rigid} , which contains rotations and translations (note that the directional vectors are invariant to translation). Variable π in (A14) is the smaller eigenvalue of the covariance matrix so that the lower bound of the anisotropic Gaussian was used to enable a simple Procrustes analysis. The rigid-body parameters were therefore computed based on singular value decomposition (Myronenko and Song, 2010; Umeyama, 1991).

Shape parameters were updated using weighted least-squares, as described in Luo and Hancock (2003). In this scheme, only the weighted sum of the squares of the residuals between rigid transformed locations and spatial MLEs were minimised:

$$\hat{\theta}_{shape} = \arg \min_{\theta_{shape}} \sum_{j=1}^M h_j^{m+1} \|\hat{\mathbf{x}}_j - T_{shape}(T_{rigid}(\mathbf{x}_j^0, \hat{\theta}_{rigid}), \theta_{shape})\|^2 \quad (\text{A15})$$

where T_{shape} applies a shape transformation of spatial locations, given the parameters θ_{shape} according to Eq. (1). It is assumed that the contribution of the shape transformation to the log-likelihood function with respect to vector reorientation is negligible in this step. Finally, we update \mathbf{x}_j by $\mathbf{x}_j^{m+1} = T_{shape}(T_{rigid}(\mathbf{x}_j^0, \theta_{rigid}), \theta_{shape})$ and re-compute \mathbf{u}_j^{m+1} using the updated \mathbf{x}_j^{m+1} and the model surface triangulations.

Although a closed-form solution to find the registration parameters in the M-step may be possible, a numerical iterative scheme is a practical method for maximising the objective function. A similar approach was described by Ziyan and Westin (2008). However, a two step update, which employs an efficient least-squares method, was developed for this application. In practice, it was found that the updated parameters increased the value of the log-likelihood function before the registration stopping criterion, based on a maximum number of iterations or a minimal change in the objective function, was reached. It should be noted that, in general, this approximation enables a fast implementation without guaranteeing convergence. Alternatively, an additional numerical optimiser could be executed after these updates in each M-step to minimise the actual log-likelihood directly.

Appendix B. RMS value of a distance error

Assuming that the errors, δ_x , δ_y , and δ_z , in each of the co-ordinates of a targeted point follow a normal distribution with zero mean and variance, σ^2 . The distance error, x , in hitting the target, given by

$$x = \sqrt{\delta_x^2 + \delta_y^2 + \delta_z^2} \quad (A16)$$

then follows a Maxwell–Boltzmann probability distribution, with probability density function

$$P(x; \sigma) = \frac{1}{\sigma^3} \sqrt{\frac{2}{\pi}} x^2 \exp \frac{-x^2}{2\sigma^2}, \quad x \in [0, \infty), \quad (A17)$$

and cumulative probability distribution

$$D(x; \sigma) = \text{erf} \left(\frac{x}{\sqrt{2}\sigma} \right) - \frac{1}{\sigma} \sqrt{\frac{2}{\pi}} x \exp \frac{-x^2}{2\sigma^2}, \quad x \in [0, \infty) \quad (A18)$$

Now, the TRE, defined as the root mean square (RMS) value of x , is given by

$$\text{TRE} = \sqrt{\int_0^\infty P(x) x^2 dx} = \sqrt{\frac{1}{\sigma^3} \sqrt{\frac{2}{\pi}} \int_0^\infty x^3 \cdot x \exp \left(\frac{-x^2}{2\sigma^2} \right) dx} \quad (A19)$$

Integrating this expression by parts, we have

$$\text{TRE} = \sqrt{\frac{1}{\sigma^3} \sqrt{\frac{2}{\pi}} \left[-\sigma^2 x^3 \exp \frac{-x^2}{2\sigma^2} \right]_0^\infty + 3\sigma^2 \int_0^\infty x^2 \exp \frac{-x^2}{2\sigma^2} dx} = \sqrt{3}\sigma \quad (A20)$$

Setting a desired hit-rate of 90% for hitting a spherical tumour region with a radius of 4.92 mm, the upper limit on σ , denoted by σ_{\max} , is given by

$$\sigma_{\max} = \arg \max_{\sigma} [D(x \leq 4.92; \sigma) \geq 0.9] \quad (A21)$$

Since D is a monotonically increasing function of x and a monotonically decreasing function of σ , we obtain:

$$\sigma_{\max} = \arg [D(x = 4.92; \sigma) = 0.9] = 1.97 \quad (A22)$$

Therefore, using the result from (A20), the corresponding TRE threshold is $\sqrt{3}\sigma_{\max} = 3.41$ mm.

References

- Ahmed, H.U., Kirkham, A., Arya, M., Illing, R., Freeman, A., Allen, C., Emberton, M., 2009. Is it time to consider a role for MRI before prostate biopsy? *Nat. Rev. Clin. Oncol.* 6 (4), 197–206.
- Ahmed, H.U., Pendse, D., Illing, R., Allen, C., van der Meulen, J.H., Emberton, M., 2007. Will focal therapy become a standard of care for men with localized prostate cancer? *Nat. Clin. Pract. Oncol.* 4 (11), 632–642.
- Ahmed, H.U., Zacharakis, E., Dudderidge, T., Armitage, J.N., Scott, R., Callear, J., Illing, R., Kirkham, A., Freeman, A., Ogden, C., Allen, C., Emberton, M., 2009a. High-intensity-focused ultrasound in the treatment of primary prostate cancer: the first UK series. *Br. J. Cancer* 101 (1), 19–26.
- Ahmed, H.U., Sahu, M., Govindaraju, S.K., Arumainayagam, N., Scott, R., Illing, R.O., Kirkham, A.P., Allen, C., Freeman, A., Van der Meulen, J., Emberton, M., 2009b. High intensity focused ultrasound (HIFU) hemiablation trial in localised unilateral prostate cancer: interim results. *Eur. Urol. Suppl.* 8 (4), 334.
- Alterovitz, R., Goldberg, K., Pouliot, J., Hsu, I.C., Kim, Y., Noworolski, S.M., Kurhanewicz, J., 2006. Registration of MR prostate images with biomechanical modeling and nonlinear parameter estimation. *Med. Phys.* 33 (2), 446–454.
- Aus, G., 2006. Current status of HIFU and cryotherapy in prostate cancer – a review. *Eur. Urol.* 50 (5), 927–934.
- Baowei, F., Corey, K., David, L.W., 2003. A comparative study of warping and rigid body registration for the prostate and pelvic MR volumes. *Comput. Med. Imag. Graph.* 267, 281.
- Barnes, A.S., Haker, S.J., Mulkern, R.V., So, M., D'Amico, A.V., Tempny, C.M., 2005. Magnetic resonance spectroscopy-guided transperineal prostate biopsy and brachytherapy for recurrent prostate cancer. *Urology* 66 (6), 1319.
- Bharatha, A., Hirose, M., Hata, N., Warfield, S.K., Ferrant, M., Zou, K.H., Suarez-Santana, E., Ruiz-Alzola, J., D'Amico, A., Cormack, R.A., Kikinis, R., Jolesz, F.A., Tempny, C.M., 2001. Evaluation of three-dimensional finite element-based deformable registration of pre- and intraoperative prostate imaging. *Med. Phys.* 28 (12), 2551–2560.
- Bilmes, J., 1997. A Gentle Tutorial on the EM Algorithm and its Application to Parameter Estimation for Gaussian Mixture and Hidden Markov Models. Technical Report ICSI-TR-97-02, U.C. Berkeley.
- Bonet, J., Burton, A.J., 1998. A simple average nodal pressure tetrahedral element for incompressible and nearly incompressible dynamic explicit applications. *Commun. Numer. Methods Eng.* 14 (5), 437–449.
- Braeckman, J., Autier, P., Garbar, C., Marichal, M.P., Soviany, C., Nir, R., Nir, D., Michielsen, D., Bleiberg, H., Egevad, L., Emberton, M., 2008. Computer-aided ultrasonography (HistoScanning): a novel technology for locating and characterizing prostate cancer. *BJU Int.* 101 (3), 293–298.
- Byrne, T.E., 2005. A review of prostate motion with considerations for the treatment of prostate cancer. *Med. Dosim.* 30 (3), 155–161.
- Clarke, D.H., Banks, S.J., Wiederhorn, A.R., Klousia, J.W., Lissy, J.M., Miller, M., Able, A.M., Artilles, C., Hindle, W.V., Blair, D.N., Houk, R.R., Sheridan, M.J., 2002. The role of endorectal coil MRI in patient selection and treatment planning for prostate seed implants. *Int. J. Radiat. Oncol. Biol. Phys.* 52 (4), 903–910.
- Cootes, T.F., Taylor, C.J., Cooper, D.H., Graham, J., 1995. Active shape models – their training and application. *Comput. Vis. Imag. Understand.* 61 (1), 38–59.
- Crouch, J.R., Pizer, S.M., Chaney, E.L., Hu, Y.C., Mageras, G.S., Zaidar, M., 2007. Automated finite-element analysis for deformable registration of prostate images. *IEEE Trans. Med. Imag.* 26 (10), 1379–1390.
- Davatzikos, C., Shen, D., Mohamed, A., Kyriacou, S.K., 2001. A framework for predictive modeling of anatomical deformations. *IEEE Trans. Med. Imag.* 20 (8), 836–843.
- Dempster, A.P., Laird, N.M., Rubin, D.B., 1977. Maximum Likelihood from Incomplete Data Via Em Algorithm. *J. Roy. Stat. Soc. Ser. B – Method.* 39 (1), 1–38.
- Descoteaux, M., Audette, M., Chinzei, K., Siddiqi, K., 2006. Bone enhancement filtering: application to sinus bone segmentation and simulation of pituitary surgery. *Comput. Aided Surg.* 11 (5), 247–255.
- du Bois, D.A., De, C.M., Haker, S., Weisenfeld, N., Tempny, C., Macq, B., Warfield, S., 2004. Improved non-rigid registration of prostate MRI. *Med. Imag. Comput. Assist. Interv. MICCAI* 2004.
- Eggner, S.E., Scardino, P.T., Carroll, P.R., Zelefsky, M.J., Sartor, O., Hricak, H., Wheeler, T.M., Fine, S.W., Trachtenberg, J., Rubin, M.A., Ohori, M., Kuroiwa, K., Rossignol, M., Abenham, L., 2007. Focal therapy for localized prostate cancer: a critical appraisal of rationale and modalities. *J. Urol.* 178 (6), 2260–2267.
- Emberton, M., et al., 2007. Phase II Clinical Trial: High-Intensity Focused Ultrasound Ablation in Treating Patients With Localized Prostate Cancer (NCT00561314).
- Epstein, J.I., Sanderson, H., Ballentine, C.H., Scharfstein, D.O., 2005. Utility of saturation biopsy to predict insignificant cancer at radical prostatectomy. *Urology* 66 (2), 356–360.
- Figueiredo, A., Gomes, P., 2006. Performance of the EM algorithm on the identification of a mixture of Watson distributions defined on the hypersphere. *Stat. J. 4* (2), 111–130.
- Frangi, A., Niessen, W., Vincken, K., Viergever, M., 1998. Multiscale vessel enhancement filtering. In: *Medical Image Computing and Computer-Assisted Intervention – MICCAI '98*, pp. 130–137.

- Futterer, J.J., 2007. MR imaging in local staging of prostate cancer. *Eur. J. Radiol.* 63 (3), 328–334.
- Haker, S., Warfield, S., Tempany, C., 2004. Landmark-guided surface matching and volumetric warping for improved prostate biopsy targeting and guidance. In: Barillot, C., Haynor, D.R., Hellier, P. (Eds.), *MICCAI 2004*, LNCS 3216, pp. 853–861.
- Halpern, E.J., Ramey, J.R., Strup, S.E., Frauscher, F., McCue, P., Gomella, L.G., 2005. Detection of prostate carcinoma with contrast-enhanced sonography using intermittent harmonic imaging. *Cancer* 104 (11), 2373–2383.
- Hambrock, T., Futterer, J.J., Huisman, H.J., Hulsbergen-vandeKaa, C., van Basten, J.P., Van, O., Witjes, J.A., Barentsz, J.O., 2008. Thirty-two-channel coil 3T magnetic resonance-guided biopsies of prostate tumor suspicious regions identified on multimodality 3T magnetic resonance imaging: technique and feasibility. *Invest. Radiol.* 43 (10), 686–694.
- Hambrock, T., Somford, D.M., Hoeks, C., Bouwense, S.A., Huisman, H., Yakar, D., van Oort, I.M., Witjes, J.A., Futterer, J.J., Barentsz, J.O., 2010. Magnetic resonance imaging guided prostate biopsy in men with repeat negative biopsies and increased prostate specific antigen. *J. Urol.* 183 (2), 520–527.
- Heimann, T., Meinzer, H.P., 2009. Statistical shape models for 3D medical image segmentation: a review. *Med. Imag. Anal.* 13 (4), 543–563.
- Hensel, J.M., Menard, C., Chung, P.W., Milosevic, M.F., Kirilova, A., Moseley, J.L., Haider, M.A., Brock, K.K., 2007. Development of multiorgan finite element-based prostate deformation model enabling registration of endorectal coil magnetic resonance imaging for radiotherapy planning. *Int. J. Radiat. Oncol. Biol. Phys.* 68 (5), 1522–1528.
- Hirose, M., Bharatha, A., Hata, N., Zou, K.H., Warfield, S.K., Cormack, R.A., D'Amico, A., Kikinis, R., Jolesz, F.A., Tempany, C.M.C., 2002. Quantitative MR imaging assessment of prostate gland deformation before and during MR imaging – guided brachytherapy. *Acad. Radiol.* 9, 906–912.
- Hu, Y., Morgan, D., Ahmed, H.U., Pendse, D., Sahu, M., Allen, C., Emberton, M., Hawkes, D., Barratt, D., 2008. A statistical motion model based on biomechanical simulations for data fusion during image-guided prostate interventions. *Med. Imag. Comput. Assist. Interv. Int. Conf.* 11 (Pt 1), 737–744.
- Hu, Y., Morgan, D., Ahmed, H., Pendse, D., Sahu, M., Allen, C., Emberton, M., Hawkes, D., Barratt, D., 2008b. Modelling prostate gland motion for image-guided interventions. In: *Biomedical Simulation*, Springer, pp. 79–88.
- Jemal, A., Siegel, R., Ward, E., Hao, Y., Xu, J., Thun, M.J., 2009. Cancer statistics, 2009. *CA Cancer J. Clin.* 59 (4), 225–249.
- Joldes, G.R., Wittek, A., Miller, K., 2009. Non-locking tetrahedral finite element for surgical simulation. *Commun. Numer. Methods Eng.* 25 (7), 827–836.
- Kaplan, I., Oldenburg, N.E., Meskell, P., Blake, M., Church, P., Holupka, E.J., 2002. Real time MRI-ultrasound image guided stereotactic prostate biopsy. *Magn. Reson. Imag.* 20 (3), 295–299.
- Kirkham, A.P., Emberton, M., Allen, C., 2006. How good is MRI at detecting and characterising cancer within the prostate? *Eur. Urol.* 50 (6), 1163–1174.
- Klein, S., van der Heide, U.A., Lips, I.M., Van, V.M., Staring, M., Pluim, J.P., 2008. Automatic segmentation of the prostate in 3D MR images by atlas matching using localized mutual information. *Med. Phys.* 35 (4), 1407–1417.
- Lattouf, J.B., Grubb III, R.L., Lee, S.J., Bjurlin, M.A., Albert, P., Singh, A.K., Ocak, I., Choyke, P., Coleman, J.A., 2007. Magnetic resonance imaging-directed transrectal ultrasonography-guided biopsies in patients at risk of prostate cancer. *BJU Int.* 99 (5), 1041–1046.
- Lindner, U., Lawrentschuk, N., Trachtenberg, J., 2010. Focal laser ablation for localized prostate cancer. *J. Endourol.* 24 (5), 791–797.
- Lindner, U., Weersink, R.A., Haider, M.R., Gertner, M.R., Davidson, S.R., Atri, M., Wilson, B.C., Fenster, A., Trachtenberg, J., 2009. Image guided photothermal focal therapy for localized prostate cancer: phase I trial. *J. Urol.* 182 (4), 1371–1377.
- Luo, B., Hancock, E.R., 2003. A unified framework for alignment and correspondence. *Comput. Vis. Imag. Understand.* 92 (1), 26–55.
- McNeal, J.E., Redwine, E.A., Freiha, F.S., Stamey, T.A., 1988. Zonal distribution of prostatic adenocarcinoma: correlation with histologic pattern and direction of spread. *The American Journal of Surgical Pathology* 12.
- Makni, N., Puech, P., Lopes, R., Dewalle, A.S., Colot, O., Betrouni, N., 2009. Combining a deformable model and a probabilistic framework for an automatic 3D segmentation of prostate on MRI. *Int. J. Comput. Assist. Radiol. Surg.* 4 (2), 181–188.
- Marberger, M., Carroll, P.R., Zelefsky, M.J., Coleman, J.A., Hricak, H., Scardino, P.T., Abenhaim, L.L., 2008. New treatments for localized prostate cancer. *Urology* 72 (6 Suppl.), S36–S43.
- Mohamed, A., Davatzikos, C., Taylor, R., 2002. A combined statistical and biomechanical model for estimation of intra-operative prostate deformation. *Med. Imag. Comput. Assist. Interv.*, 452–460.
- Moradi, M., Mousavi, P., Abolmaesumi, P., 2007. Computer-aided diagnosis of prostate cancer with emphasis on ultrasound-based approaches: a review. *Ultrasound Med. Biol.* 33 (7), 1010–1028.
- Myronenko, A., Song, X., Carreira-Perpinan, M.A., 2006. Non-rigid Point Set Registration: Coherent Point Drift. *Advances in Neural Information Processing Systems* 19, (NIPS 2006), MIT Press.
- Myronenko, A., Song, X., 2010. Point set registration: coherent point drift. *IEEE T. Pattern Anal.* 32 (12), 2262–2275. doi:10.1109/TPAMI.2010.46.
- Narayanan, R., Kurhanewicz, J., Shinohara, K., Crawford, E.D., Simoneau, A., Suri, J.S., 2009. MRI – ultrasound registration for targeted prostate biopsy. *Proc. ISBI* 2009, 991–994.
- Oguro, S., Tokuda, J., Elhawary, H., Haker, S., Kikinis, R., Tempany, C.M.C., Hata, N., 2009. MRI signal intensity based B-spline nonrigid registration for pre- and intraoperative imaging during prostate brachytherapy. *J. Magn. Reson. Imag.* 30, 1052–1058.
- Onik, G., Barzell, W., 2008. Transperineal 3D mapping biopsy of the prostate: an essential tool in selecting patients for focal prostate cancer therapy. *Urol. Oncol.* 26 (5), 506–510.
- Pasquier, D., Lacornerie, T., Vermandel, M., Rousseau, J., Lartigau, E., Betrouni, N., 2007. Automatic segmentation of pelvic structures from magnetic resonance images for prostate cancer radiotherapy. *Int. J. Radiat. Oncol. Biol. Phys.* 68 (2), 592–600.
- Pinkstaff, D.M., Igel, T.C., Petrou, S.P., Broderick, G.A., Wehle, M.J., Young, P.R., 2005. Systematic transperineal ultrasound-guided template biopsy of the prostate: three-year experience. *Urology* 65 (4), 735–739.
- Pondman, K.M., Futterer, J.J., Ten, H.B., Schultze Kool, L.J., Witjes, J.A., Hambrock, T., Macura, K.J., Barentsz, J.O., 2008. MR-guided biopsy of the prostate: an overview of techniques and a systematic review. *Eur. Urol.* 54 (3), 517–527.
- Ravizzini, G., Turkbey, B., Kurdziel, K., Choyke, P.L., 2009. New horizons in prostate cancer imaging. *Eur. J. Radiol.* 70 (2), 212–226.
- Salomon, G., Kollerman, J., Thederan, I., Chun, F.K., Budaus, L., Schlomm, T., Isbarn, H., Heinzer, H., Huland, H., Graefen, M., 2008. Evaluation of prostate cancer detection with ultrasound real-time elastography: a comparison with step section pathological analysis after radical prostatectomy. *Eur. Urol.* 54 (6), 1354–1362.
- Scardino, P.T., Abenhaim, L.L., 2008. Focal therapy for prostate cancer: analysis by an international panel. *Urology* 72 (6 Suppl.), S1–S2.
- Scattoni, V., Zlotta, A., Montironi, R., Schulman, C., Rigatti, P., Montorsi, F., 2007. Extended and saturation prostatic biopsy in the diagnosis and characterisation of prostate cancer: a critical analysis of the literature. *Eur. Urol.* 52, 1309–1322.
- Schwartzman, A., Dougherty, R.F., Taylor, J.E., 2005. Cross-subject comparison of principal diffusion direction maps. *Magn. Reson. Med.* 53 (6), 1423–1431.
- Shao, W., Wu, R., Ling, K.V., Thng, C.H., Ho, H.S.S., Cheng, C.W.S., Ng, W.S., 2006. Evaluation on similarity measures of a surface-to-image registration technique for ultrasound images. In: *Medical Image Computing and Computer-Assisted Intervention – MICCAI 2006*, Springer, pp. 742–747.
- Singh, A.K., Kruecker, J., Xu, S., Glossop, N., Guion, P., Ullman, K., Choyke, P.L., Wood, B.J., 2008. Initial clinical experience with real-time transrectal ultrasonography-magnetic resonance imaging fusion-guided prostate biopsy. *BJU Int.* 101 (7), 841–845.
- Staib, L.H., Duncan, J.S., 1992. Boundary finding with parametrically deformable models. *IEEE Trans. Pattern Anal. Mach. Intell.* 14 (11), 1061–1075.
- Styner, M., Rajamani, K., Nolte, L.P., Zsemlye, G., Székely, G.A., Taylor, C., Davies, R., 2003. Evaluation of 3D correspondence methods for model building. *Inform. Process. Med. Imag.*, 63–75.
- Taylor, Z.A., Cheng, M., Ourselin, S., 2008. High-speed nonlinear finite element analysis for surgical simulation using graphics processing units. *IEEE Trans. Med. Imag.* 27 (5), 650–663.
- Tempany, C., Straus, S., Hata, N., Haker, S., 2008. MR-guided prostate interventions. *J. Magn. Reson. Imag.* 27 (2), 356–367.
- Terris, M.K., Wallen, E.M., Stamey, T.A., 1997. Comparison of mid-lobe versus lateral systematic sextant biopsies in the detection of prostate cancer. *Urol. Int.* 59 (4), 239–242.
- Thompson, S., Thompson, S., Penney, G., Penney, G., Buie, D., Buie, D., Dasgupta, P., Dasgupta, P., Hawkes, D., Hawkes, D., 2008. Use of a CT statistical deformation model for multi-modal pelvic bone segmentation. *Proc. SPIE* 6914 (1).
- Trachtenberg, J., Weersink, R.A., Davidson, S.R., Haider, M.A., Bogaards, A., Gertner, M.R., Evans, A., Scherz, A., Savard, J., Chin, J.L., Wilson, B.C., Elhilali, M., 2008. Vascular-targeted photodynamic therapy (padoporfin, WST09) for recurrent prostate cancer after failure of external beam radiotherapy: a study of escalating light doses. *BJU Int.* 102 (5), 556–562.
- Umeyama, S., 1991. Least-squares estimation of transformation parameters between 2 point patterns. *IEEE Trans. Pattern Anal. Mach. Intell.* 13 (4), 376–380.
- Villers, A., Lemaitre, L., Haffner, J., Puech, P., 2009. Current status of MRI for the diagnosis, staging and prognosis of prostate cancer: implications for focal therapy and active surveillance. *Curr. Opin. Urol.* 19 (3), 274–282.
- Villers, A., Puech, P., Mouton, D., Leroy, X., Ballereau, C., Lemaitre, L., 2006. Dynamic contrast enhanced, pelvic phased array magnetic resonance imaging of localized prostate cancer for predicting tumor volume: correlation with radical prostatectomy findings. *J. Urol.* 176 (6 Pt 1), 2432–2437.
- Watson, G.S., 1983. *Statistics on Spheres*. Wiley, New York.
- Weinreb, J.C., Blume, J.D., Coakley, F.V., Wheeler, T.M., Cormack, J.B., Sotto, C.K., Cho, H., Kawashima, A., Tempany-Afdhal, C.M., Macura, K.J., Rosen, M., Gerst, S.R., Kurhanewicz, J., 2009. Prostate cancer: sextant localization at MR imaging and MR spectroscopic imaging before prostatectomy – results of ACRIN prospective multi-institutional clinicopathologic study. *Radiology* 251 (1), 122–133.
- Wu, R., Ling, K.V., Shao, W., Ng, W.S., 2003. Registration of organ surface with intra-operative ultrasound image using genetic algorithm. In: *Medical Image Computing and Computer-Assisted Intervention – MICCAI 2003*, Springer, pp. 383–390.
- Xu, S., Kruecker, J., Turkbey, B., Glossop, N., Singh, A.K., Choyke, P., Pinto, P., Wood, B.J., 2008. Real-time MRI-TRUS fusion for guidance of targeted prostate biopsies. *Comput. Aided Surg.* 13 (5), 255–264.
- Yang, J.C., Tang, J., Li, J., Luo, Y., Li, Y., Shi, H., 2008. Contrast-enhanced gray-scale transrectal ultrasound-guided prostate biopsy in men with elevated serum prostate-specific antigen levels. *Acad. Radiol.* 15 (10), 1291–1297.

- Zacharopoulos, A.D., Arridge, S.R., Dorn, O., Kolehmainen, V., Sikora, J., 2006. Three-dimensional reconstruction of shape and piecewise constant region values for optical tomography using spherical harmonic parametrization and a boundary element method. *Inverse Probl.* 22 (5), 1509–1532.
- Zhang, M., Nigwekar, P., Castaneda, B., Hoyt, K., Joseph, J.V., Di, S.A., Messing, E.M., Strang, J.G., Rubens, D.J., Parker, K.J., 2008. Quantitative characterization of viscoelastic properties of human prostate correlated with histology. *Ultrasound Med. Biol.* 34 (7), 1033–1042.
- Zienkiewicz, O.C., Taylor, R.L., 2000. *The Finite Element Method*. Butterworth, Heinemann.
- Ziyan, U., Westin, C.F., 2008. Joint segmentation of thalamic nuclei from a population of diffusion tensor MR images. *Med. Imag. Comput. Comput. Assist. Interv. Int. Conf.* 11 (Pt 1), 279–286.